# Induction of a strong and long-lasting neutralizing immune response by dPreS1-TLR2 agonist nanovaccine against hepatitis B virus

Myriam Lamrayah, Fanny Charriaud, Manon Desmares, Céline Coiffier, Simon Megy, Evelyne Colomb, Raphaël Terreux, Julie Lucifora, David Durantel, Bernard Verrier

# Induction of a strong and long-lasting neutralizing immune response by dPreS1-TLR2 agonist nanovaccine against Hepatitis B Virus

**Authors**

Myriam Lamrayah[a], Fanny Charriaud[a], Manon Desmares[b], Céline Coiffier[a], Simon Megy[c], Evelyne Colomb[a], Raphaël Terreux[c], Julie Lucifora[b], David Durantel[b], Bernard Verrier[a]

[a] Colloidal vectors and therapeutic targeted engineering, UMR5305, LBTI, Institut de Biologie et Chimie des Protéines, Université Lyon 1, 7 Passage du Vercors, 69367 Lyon Cedex 07, France.

[b] HepVir team, Centre International de Recherche en Infectiologie (CIRI), INSERM U1111, CNRS UMR_5308, University of Lyon (UCBL1), Lyon, France

[c] ECMO team, UMR5305, LBTI, Institut de Biologie et Chimie des Protéines, Université Lyon 1, 7 Passage du Vercors, 69367 Lyon Cedex 07, France.

* Corresponding author : School of Life Sciences, Ecole Polytechnique Fédérale de Lausanne, SV Station 19, 1015 Lausanne, Switzerland. E-mail address : myriam.lamrayah@epfl.ch.

**Abstract**

Hepatitis B virus remains a major medical burden with more than 250 million chronically infected patients worldwide and 900,000 deaths each year, due to the disease progression towards severe complications (cirrhosis, hepatocellular carcinoma). Despite the availability of a prophylactic vaccine, this infection is still pandemic in Western Pacific and African regions, where around 6% of the adult population is infected. Among novel anti-HBV strategies, innovative drug delivery systems, such as nanoparticle platforms to deliver vaccine antigens or therapeutic molecules have been investigated. Here, we developed polylactic acid-based biodegradable nanoparticles as an innovative and efficient vaccine. They are twice functionalized by (i) the entrapment of $Pam_3CSK_4$, an immunomodulator and ligand to Toll-Like-Receptor 1/2, and by (ii) the adsorption/coating of myristoylated (2-48) derived PreS1 from the HBV surface antigen, identified as the major viral attachment site on hepatocytes. We demonstrate that such formulations mimic HBV virion with an efficient peptide recognition by the immune system, and elicit potent and durable antibody responses in naive mice during at least one year. We also show that the most efficient *in vitro* viral neutralization was observed with NP-$Pam_3CSK_4$-dPreS1 sera. The immunogenicity of the derived HBV antigen is modulated by the likely synergistic action of both the dPreS1 coated nanovector and the adjuvant moiety. This formulation represents a promising vaccine alternative to fight HBV infection.

**Keywords**

Hepatitis B virus, neutralizing antibodies, PreS1 peptide, TLR agonist, nanoparticle, poly(lactic acid)

**Highlights**

- PreS1 peptide derived from HBV surface protein was successfully adsorbed on PLA NP
- Vectorized $Pam_3CSK_4$ does not influence the colloidal characteristics of NP-dPres1
- NP-dPreS1 activates murine lymph nodes after subcutaneous administration
- $Pam_3CSK_4$ adjuvant positively modulates the quality of immune response triggered by NP
- NP-$Pam_3CSK_4$-dPreS1 induces the most efficient murine IgG for *in vitro* neutralization

## 1. Introduction

Nearly 3.5% of the world population suffer from chronic hepatitis B virus (HBV) (Polaris Observatory Collaborators, 2018) and predictions for the future are not optimistic, as the mortality rate is increasing and outweighing those of tuberculosis, malaria, and HIV (Bray et al., 2018; Graber-Stiehl, 2018). Even though existing prophylactic vaccines widely protect the rich countries benefiting from it, they present some drawbacks that make it difficult to implement in developing countries: cold storage, a strict three-shot immunization schedule, the failing to induce an effective antibody (Ab) response in 5-10% of healthy “non responders” (Saco et al., 2018) and the emergence of vaccine escape strains (Qin and Liao, 2018). New potent vaccines have to be considered via (i) the use of drug delivery systems to optimize the administration (Zhu et al., 2019), (ii) the modification of the antigen (Ag) sequence for a more immunogenic portion, (iii) the adjuvantation to enhance the immune response (Fanning et al., 2019; Lang et al., 2019; Meng et al., 2019). This has been confirmed recently in the course of SARS-CoV-2 countermeasures, when the numerous failed clinical trials have highlighted the importance to generate innovative and highly-immunogenic formulations through efficient systems (Monrad et al., 2021; Peplow, 2021).

Multiple drug delivery systems (*i.e.* virus-like particles, nanoparticles) and innovative gene-based formulations (DNA/RNA vaccines) have been largely exploited in vaccinology for their added value compared to a conventional soluble Ag (Fries et al., 2020) and thus, for their ability to face a global health emergency, such as the ongoing SARS-CoV-2 pandemic (Brisse et al., 2020). Nanoparticle (NP) systems aim at overcoming the limitations of conventional delivery by : improving the stability and solubility of molecules, facilitating the transport across membranes to modulate the traffic and the delivery of vaccine components throughout the lymphatic tissue (Mitchell et al., 2020; Schudel et al., 2019), thus improving the Ag presentation and overall the prophylactic activity (Fries et al., 2020). By efficiently targeting the lymph nodes (LN), nanovaccines induce a more persistent B cell immune response compared to conventional forms (Singh, 2021). Biodegradable polymeric NP are one of the most extensively studied in the field for their low immunogenicity and biocompatibility and our previous results showed the polylactic acid (PLA) as a great polymer candidate for such scaffolds (Coolen et al., 2019; Pavot et al., 2016; Rességuier et al., 2017). They offer a versatile platform for vectorization (Pavot et al., 2013) and/or adsorption (Dalzon et al., 2016) of various molecules (Ag, immunomodulators) and are promising candidates for vaccine development (Gutjahr et al., 2016; Peres et al., 2017).

Yan *et al* elegantly identified the myristoylated oligopeptide (amino acids sequence 2-48) named PreS1 from the large surface protein, as the molecule enabling HBV to enter into the hepatocyte (Yan et al., 2012) through a high-affinity binding with the sodium taurocholate cotransporting polypeptide (NTCP) receptor (Meier et al., 2013). The inhibition of this PreS1-NTCP interaction effectively blocks HBV and hepatitis D virus (HDV) infections (Ni et al., 2014; Ye et al., 2016). Bulevirtide (also known as myrcludex B), the GMP-version of the myristoylated (2-48) PreS1, was recently approved in Europe for HDV treatment (Cheng et al., 2021). Yato *et al* suggested the potential ability of a vaccine Ag containing the preS1 region to overcome the weakness of current hepatitis B vaccines (Yato et al., 2020). Indeed, monoclonal Abs against the conventional HBsAg protein cannot neutralize HBV in case of vaccine escape mutations such as the G145R mutation which causes a conformational change in the HBsAg antigenic loop. This lack of neutralization is not observed with Abs against PreS1/2-48. Two other studies recently highlighted also the added value of using this PreS1 domain by bypassing the host immune tolerance observed with HBsAg vaccines (Bian et al., 2017; Dembek et al., 2018). Inducing specific anti-PreS1 Abs may therefore be optimal when the conventional HBV vaccine targeting the main antigenic region (AR). Here, a derived PreS1 (dPreS1) sequence of the virus was successfully nanovectorized in PLA NP and investigated.

As an adjuvant, the Toll-Like-Receptor (TLR) 1/2 agonist $Pam_3CSK_4$ was included in the nanosystem for an enhanced magnitude and durability of the immune response (Pulendran et al., 2021). The literature demonstrates the efficacy of synthetic TLR ligands on rodents and non-human primates by promoting a more durable and stronger Ab response to vaccination with live or heat-killed viruses (Hennessy et al., 2010; Kasturi et al., 2011). More specifically for HBV, Heplisav-B is an FDA-approved vaccine composed of HBsAg mixed with a synthetic oligonucleotide cytosine phosphor-guanine (CpG) that stimulate innate immunity through TLR9 (Lee and Lim, 2021). In case of TLR2, multiple experimental evidences show the promising adjuvanticity of $Pam_3$-related ligands as strong inducers of virus-specific T and B cells in mice (Dou et al., 2020; Lee and Park, 2018; Rammensee et al., 2019). Desmares *et al* (Desmares et al., 2022) illustrate recently the direct inhibitory anti-HBV phenotypes induced by this TLR2 ligand itself supporting our assumption of an added value in using $Pam_3CSK_4$. Despite the numerous preclinical and clinical studies applied to TLR ligands, their mechanisms of action suggest failures related to toxicity issues limiting a human use (Anwar et al., 2019).

For all these reasons, we propose a highly immunogenic doubly-functionalized NP vaccine against HBV, incorporating both the unique dPreS1 domain and a TLR1/2 ligand for adjuvanticity. We have previously discussed the successful chemical entrapment of $Pam_3CSK_4$ in PLA NP (Lamrayah et al., 2019). Here, in order to validate the immunological relevance and the effective design of our NP-dPreS1vaccine, we first performed *in silico* structural and physicochemical modulations. Then, the immune responses elicited by a prime-boost administration were evaluated in comparison with different formulations. The NP-$Pam_3CSK_4$-dPreS1 (hereafter designated NP-P-dPreS1) system aims at stimulating the production of neutralizing Abs directed specifically against the dPreS1 epitope all the while favorably modulating the immune response for an optimal immune protection. Finally, the *in vitro* neutralization capacity of the generated antibodies was tested to evaluate their antiviral efficacy. Overall, this work offers a promising platform for a novel anti-HBV vaccine and maybe a potential strategy to achieve a functional cure in a therapeutic context, as it induces a high level and persistent anti-PreS1 response that could help in clearing circulating HBV virions as well as infected hepatocytes *in vivo* by various mechanisms (e.g., neutralization, ADCC, etc..).

## 2. Materials and methods

### 2.1. Preparation and characterization of formulations

PLA NP were prepared by nanoprecipitation technique as previously described (Lamalle-Bernard et al., 2006). Briefly, the polymer was dissolved in acetone and this solution was added dropwise to an aqueous solution under 250 rpm stirring. Organic solvents were then removed under reduced pressure at 30°C with a Rotavapor R-300 (Buchi, France).

$Pam_3CSK_4$ (purchased from InvivoGen, San Diego, CA, USA) was incorporated during the NP synthesis, following the procedure already described (Lamrayah et al., 2019). The final concentration of $Pam_3CSK_4$ was 2.5 µg/injection.

The near infrared DiR XenoLight Fluorescent Dye (DiIC18(7), 1,1'-dioctadecyltetramethyl indotricarbocyanine Iodide), purchased from Perkin Elmer (Waltham, MA, USA), was incorporated during the NP synthesis step at a fluorophore:PLA ratio of 0.02% and was manufactured by Adjuvatis (Lyon, France).

The 2-48 AA sequence of the HBV PreS1 peptide with a myristoylation in N-terminal (GTNLSVPNPLGFFPDHQLDPAFRANSNNPDWDFNPNKDHWPEANKVG) was produced by GenScript Biotech (Piscataway, NJ, USA). The purity was higher than 98% and the observed

molecular weight was 5499.5 g/mol. For the preparation of dPreS1 PLA NP, the lyophilized dPreS1 was rehydrated in PBS 1X (Thermo Fisher Scientific, Waltham, MA, USA) at the desired concentration and added volume to volume in NP, NP(DiR) or NP-$Pam_3CSK_4$ suspensions, previously diluted at 20 mg/mL of polymer in DPBS 1X. The passive adsorption reaction occurred within 2 h at room temperature with moderate overhead stirring. The coating efficiency was assessed by measuring the unbound peptide. A certain volume of dPreS1 PLA NP was centrifuged 15 min at 15,000 xg and the absorbance of the supernatant was measured at 280 nm using a Tecan i-control Infinite M1000 (Tecan, Männedorf, Switzerland). The results were compared to a calibration curve previously established (correlation coefficient of $R^2$=0.998). The encapsulation efficiency was calculated as the following formula: EE (%) = (1 - amount of dPreS1 in supernatant / Total amount of dPreS1) x 100. The final concentration of dPreS1 was 20 µg/injection.

The average hydrodynamic diameter and the size distribution (mentioned as polydispersity index or PDI) of formulations were determined by dynamic light scattering at 25°C and a scattering angle of 173° using a Zetasizer Nano ZS (Malvern, UK). The colloidal suspensions were a hundred time diluted in filtrated 1 mM NaCl solution and each value was the mean of four independent measurements. The electrophoretic mobilities (mentioned as zeta potential) were measured by laser Doppler velocimetry using the same equipment, at a scattering angle of 12.5°.

For KLH-dPreS1 formulation, 200 µg of dPreS1 was conjugated with 200 µg of mariculture Key Limpet Hemocyanin (mcKLH) in EDC conjugation buffer, following the manufacturer's instructions (Imject™ EDC mcKLH Spin Kit, Thermo Fisher Scientific, USA). The mix was incubated for 2 h statically at room temperature. The conjugate was purified by successive desalting steps to remove the non-reacted crosslinker.

### 2.2. Molecular Modeling

MD simulations were performed using the Amber 14 force field implemented in the Molecular Operating Environment (MOE) software (ChemComp). This type of atomistic simulation allows for the modeling of various system sizes but is less efficient with larger systems, especially when the total number of atoms reaches millions, which is the amount typically found in a 150 nm diameter NP. Thus, in order to mimic the behavior of a PLA NP while keeping the total number of atoms in the simulation under a reasonable limit, we chose to use instead a smooth flat layer of PLA with a 35 Å thickness, located in a replicative cell measuring 60x60x120 Å. To simulate the NP PLA surface, we used PLA molecules constructed as linear repetitions of 50 units of Lactic Acid monomers (LA). Those molecules were generated using the "Build" module of the Material Studio software (Biovia). Water molecules were added for the solvation of the replicative cell. The simulation box was then thoroughly minimized using the Forcite module of Material Studio. The PLA molecules and the replicative cell were then exported in .pdb format and imported into the MOE software. Then, a molecular model of the dPreS1 peptide was constructed. As no single relevant template could be found in the PDB database, we used the online software I-TASSER (Iterative Threading ASSEmbly Refinement) from the Zhang Lab ("I-TASSER server for protein structure and function prediction," n.d.). Five models were computed using the software default options, and the best one was further imported into MOE. The lipidic myristoyl anchor of dPreS1 was constructed using the MOE Build module and the molecule was briefly minimized using the Amber 14 EHT force field. The final model was added to the PLA periodic cell and located close to the PLA surface. The geometry of all the molecules, bonds and charges were checked using the Structure Preparation tool in MOE, to start molecular simulations. Water molecules, $Na^+$ and $Cl^-$ ions were added to simulate a 0.1 M ionic force, and pH was set at 7.4. The total number of atoms in the simulation cell was 38,403. Standard Amber 14 EHT parameters were used for the molecular dynamics. A quick minimization was performed prior to the start of the MD simulations. After a

preliminary equilibration phase, a 200 ns molecular simulation was performed. A frame was saved every 20 ps, leading to a total number of 10,000 frames.

### 2.3. Docking

The docking experiments were performed between the CSKKKK peptidic part of the $Pam_3CSK_4$ lipopeptide and the 47 AA sequence of PreS1. The protocol involved a first global approach step of peptide/protein docking using the Haddock (High Ambiguity Driven protein-protein DOCKing) web server (van Zundert et al., 2016) and the Cluspro 2.0 web server ("ClusPro 2.0: protein-protein docking," n.d.). No constraints about the binding area were specified and all the residues of the CSKKKK peptide were treated as flexible. The two servers produced 42 poses, which were selected and sent for further docking refinement to the Rosetta docking software, version 3.12 (Chaudhury and Gray, 2008). All initial Haddock and Cluspro pose were refined 100 times with Rosetta, leading to 4200 refined poses. The top ten results were evaluated with the Rosetta 2015 scoring function (Park et al., 2016) and exhibited a mean average reweighted score of 60.1 Rosetta Energy Units.

### 2.4. Electron microscopy observations

Morphology of formulations was visualized through a transmission electron microscope (JEM-2100F, JEOL, Japan). For sample preparation, NP solutions were diluted ten times in water and deposited on a grid. The excess liquids were absorbed using filter paper and the grids were negatively stained by sodium silicotungstate for contrast. Images were recorded at a magnification between x10K and x20K.

### 2.5. *In vivo* imaging of fluorescent NP biodistribution

Ten-week-old SKH1 female mice (n=4 per group) were bred at Charles River Laboratories (L'Arbresle, France) and housed at the AniCan animal facility of the CRCL (Cancer Research Center of Lyon, France). The experiments were approved by the relevant local ethics committee (CECCAPP_CLB_2017_006) and were conducted according to the rules for the care and use of laboratory animals. The mice received a single subcutaneous injection in the neck of 0.96 µM DiR/mouse loaded in NP or in dPreS1-NP, corresponding to 20 µg of dPreS1/mouse (injection volume: 100 µl). Whole body fluorescence was recorded at determined time points (2, 24 h and 7 days after injection) using the FMT4000 fluorescence tomography imaging system (Perkin Elmer, USA). On the day of imaging, mice were anesthetized under 4% isoflurane and positioned in the FMT system imaging chamber. Filter set was chosen depending on the fluorophore parameters, with an excitation at 750 nm and a collection at 782 nm. The collected fluorescence data were reconstructed by TrueQuant software for the quantification of three-dimensional fluorescence signals. Acquired images were analyzed by drawing regions of interest (ROI). The total amount of fluorescence (in pmoles) per ROI was generated for all studies, and then percentage of residual fluorescence was calculated as: residual fluorescence (%) = [amount of fluorescence at tx / amount of fluorescence at t0] x 100.

### 2.6. Lymph nodes immunofluorescence staining

Seven-to-eight-week-old mice were divided into five groups of nine animals and received a single immunization of the different formulations in a 100 µl final volume of PBS 1X, subcutaneously above the left inguinal LN. Mice were retro-orbitally bled before immunization and 7-, 14-, 21- and 28-days post-immunization. Three mice of each group were euthanized at 7-, 14-, 21- and 28-days post-immunization to harvest the draining inguinal LNs. They were snap frozen in cryomolds full of

Optimal Cutting Temperature compound (Tissue-Tek O.C.T, Sakura Finetek, USA) placed on dry ice and stored at -80°C until cryosection. Serial sections, 8 µm thick, were collected through each LN using a cryostat microtome (cryostat CM3050, Leica Biosystems, Germany). The central section and the two sections spaced 250 µm apart were fixed on glass slides with acetone. They were first incubated with a rat anti-mouse IgD primary Ab (Biolegend, San Diego, CA, USA) to detect B cells follicles and with biotinylated PNA (Vectors Laboratories, Burlingame, CA, USA) to detect GC. They were then incubated with goat anti-rat IgG secondary Ab conjugated with Alexa Fluor 488 (Thermo Scientific, Rockford, IL, USA) to reveal anti-IgD (green), and with Streptavidin conjugated with DyLight 550 (Thermo Scientific, Rockford, IL, USA) to reveal biotinylated PNA (red). Images of LN sections were captured using an inverted microscope (Nikon Ti-E microscope, Nikon Instruments Inc., Melville, NY, USA) equipped with a 4x objective. Measurements of B cells and GCs areas were carried out using Image J software (U. S. National Institutes of Health, Bethesda, MD, USA). GCs were manually counted.

### 2.7. CXCL13 ELISA

The mouse CXCL13/BLC/BCA-1 DuoSet (R&D Systems, USA) was used for quantification of CXCL13 in sera samples, according to the manufacturer's recommendations. Briefly, ninety-six-well Nunc maxisorp plates were coated with 100 µL of Capture Ab at 1 µg/mL, overnight at room temperature. Capture Ab excess was eliminated and plates were washed 3 times with PBS/0.05% Tween-20 (PBS-T20) using a Thermo Scientific autoplate washer. Plates were blocked with 300 µL of Block buffer (R&D Systems, USA) for 1 h at room temperature, to prevent non-specific binding of the CXCL13 protein. Fresh serum samples from immunized mice were diluted five times in Reagent Diluent (RD) (R&D Systems, USA). A seven-point standard range using two-fold serial dilutions in RD of the recombinant mouse BLC/BCA-1 Standard was realized. Then, 100 µL of each sample and standard in duplicate were incubated on washed plates for 2 h at room temperature. Wells were washed and incubated 2 h at room temperature with Detection Ab diluted at 25 ng/mL in RD. Plates were washed again and incubated with 100 µL per well of diluted Streptavidin-HRP in RD (1:200) for 20 min at room temperature, in the dark. Plates were washed again, revealed using 100 µL per well of tetramethylbenzidine (TMB) substrate (BD BioSciences, USA) and stopped using 2N $H_2SO_4$ (Merck, USA). The optical density (OD) at 450 nm ($OD_{450}$) with a correction at 620 nm was measured using a Thermo Scientific plate reader spectrophotometer.

### 2.8. Immune evaluation of formulations in naive mice

CB6F1 female mice were bred at Charles River Laboratories (L'Arbresle, France) and housed at the Plateau de Biologie Expérimentale de la Souris (PBES, Lyon, France). The experiments were approved by the relevant local ethics committee (CECCAPP_ENS_2017_017) and were conducted according to the rules for the care and use of laboratory animals.

Seven-to-eight-week-old mice were equally distributed into six groups in the indicated experimental groups. They were subcutaneously immunized (above the left inguinal LN) with NP-dPreS1, NP-$Pam_3CSK_4$-dPreS1, soluble dPreS1, NP as negative control and KLH-dPreS1 as positive control. The injection scheme followed a prime boost injection strategy, based on Aditec consortium protocol for harmonization with three immunizations each three weeks. A sixth group received a retro-orbitally intravenous injection of NP-$Pam_3CSK_4$-dPreS1, following the same scheme of immunization. Components were administered equally for each group, namely 2.5 µg of dPreS1, 20 µg of $Pam_3CSK_4$, 10 mg/mL of PLA and all formulations were diluted in PBS 1X for a 100 µl final volume of injection.

Then, a heterologous boost was performed at W27, with a unique formulation subcutaneously injected for all groups, meaning dPreS1 NP. Control groups received a homologous injection,

meaning NP and KLH-dPreS1 respectively as negative and positive controls, to maintain the reference consistent.

Mice were retro-orbitally bled before immunization and at determined times (W2, 4, 6, 8, 11, 13, 17, 22, 27, 32, 44 and 47 weeks post-immunization). The blood samples were heated 30 min at 37°C for coagulation, then centrifuged twice 10 min at 16,000 ×g and sera were stored at −20°C for further analyses. Mice were weighted regularly to verify the potential general toxicity of immune stimulation in naive organisms and the evolution rate for each group was measured as: ((W47 weight - W7 weight)/ W7 weight) x 100 = evolution rate (%). Mice were sacrificed at W47 by cervical dislocation.

### 2.9. dPreS1 specific IgG ELISA

Collected sera were tested for the quantification of dPreS1 specific IgG, IgG1 and IgG2a by enzyme-linked immunosorbent assay (ELISA). Ninety-six-well Nunc maxisorp plates (ThermoFisher Scientific, USA) were coated with 100 µL of dPreS1 at 1 µg/mL, overnight at room temperature. The dPreS1 excess was eliminated and plates were blocked with 200 µL of 10% non-fat dry milk in PBS for 1 h at 37°C to prevent non-specific binding of the Abs. Plates were washed 3 times with PBS/0.05% Tween-20 (PBS-T20) using a Thermo Scientific autoplate washer. Serum samples from immunized mice were serially diluted in Dulbecco's PBS (DPBS) containing 1% (w/w) of Bovine Serum Albumin (Euromedex, Souffelweyersheim, France). Then, 100 µL of each sample in duplicate were incubated on blocked plates for 1 h at 37°C. Wells were washed three times and incubated 1 h at 37°C with anti-mouse IgG-HRP (horseradish peroxidase) conjugate (1:10,000) from Southern Biotech, Birmingham, AL, USA (ref 1030-05). Plates were washed again, revealed using 100 µL per well of tetramethylbenzidine (TMB) substrate (BD Biosciences, USA) and stopped using 1N sulfuric acid. The optical density (OD) at 450 nm with a correction at 620 nm was measured using a microplate reader spectrophotometer (Multiskan FC, Thermo Fisher, USA). The limit of detection was evaluated using an unconjugated mouse monoclonal anti-Hep B PreS1 (ref SC-57761) from Santa Cruz Biotechnology, Inc. (Dallas, TX, USA).

Sera from W0, 11, 22, 32 and 47 were also evaluated for the presence of dPreS1 specific IgG1 and IgG2a, using the same protocol than for total IgG, except the last incubation with IgG1-HRP (ref 1070-05) or IgG2a-HRP (ref 1080-05) conjugate, both from Southern Biotech.

The avidity indices of IgG at W6, 11, 22, 32 and 47 were determined by the Ab-Ag binding resistance to 8M of urea. Samples were prediluted to give an $OD_{450}$ readout of between 1.0 and 1.5, with a correction at 620 nm, and were added to dPreS1 coated plates. Then, they were washed three times with either PBS-T20 or 8 M urea in PBS-T20, before incubating with anti-mouse IgG-HRP. Samples were developed with TMB as described above. The avidity index (in percent) was calculated as the ratio of absorbance of bound Ag in the plate with and without urea as denaturing reagent = (OD urea/OD PBS-T20) x 100. Index values exceeding 50% were ascribed a high avidity, those between 30 and 50% were ascribed intermediate avidity, and those below to 30% were ascribed a low avidity.

### 2.10. Cell culture

*In vitro* experiments were performed with a HepaRG cell line (Gripon et al., 2002). Cells were maintained in William's E medium (Life technologies, USA) supplemented with 10% fetal calf serum (FCS) (Eurobio, Hyclone), 100 U/mL of penicillin and 100 µg/mL streptomycin (Gibco, Life technologies, USA), 2 mM GlutaMAX (Gibco, Life technologies, USA), 5 µg/mL of human insulin solution (Sigma-Aldrich, USA) and $5.10^{-5}$ M hydrocortisone hemisuccinate (Serb, France) at 37°C

in humidified incubator and 5% $CO_2$ for two weeks. Two additional weeks are needed for differentiation in standard medium supplemented with 1.8% DMSO (Sigma-Aldrich, MO, USA).

### 2.11. Neutralization of HBV by mice antisera

Sera from W11, 27 and 47 were diluted into infectious mediums. This last medium was prepared using a differentiation medium containing 4% PEG 8000 (Sigma-Aldrich, MO, USA) and infected with HBV genotype D inoculum prepared from HepAD38 (Lucifora et al., 2018). The infectious medium containing immunized mice sera were maintained during 16 h on HepaRG cells at 37°C and 5% $CO_2$. Cells were then washed with PBS and the medium of differentiation was added. All *in vitro* experiments were stopped one week after infection and treatment with immunized mice sera. Myrcludex was used as positive control (0.5 ng/mL and 5 ng/mL) after determination of IC50 and IC90 on studied cell lines.

### 2.12. HBe antigen ELISA

From cell culture supernatants, secreted HBeAg and the amount produced were analyzed by ELISA, using a chemiluminescence immunoassay kit (Autobio, China) according to the manufacturer's instructions.

### 2.13. Statistical analyses

Statistical analyses were performed using GraphPad Prism Version 9.0 software. For each dataset, normality or lognormality was assessed via d'Agostino & Pearson test or Shapiro-Wilk when n was too small and further analyzed accordingly. $P<0.05$ was considered significant. Differences between groups were analyzed as described in figure legends.

## 3. Results

### 3.1. Design and molecular dynamics studies of HBV-specific NP formulations

PLA NP were prepared according to an adjuvant-free nanoprecipitation method (Lamalle-Bernard et al., 2006) and $Pam_3CSK_4$ was simultaneously entrapped in PLA NP as previously described (Lamrayah et al., 2019). Secondly, dPreS1 peptide (2-48 AA construct from a consensus sequence with a N-terminal myristoylation) was added at the surface of the NP by passive adsorption (Dalzon et al., 2016; Pavot et al., 2016). The functionalization of PLA NP by $Pam_3CSK_4$ and dPreS1 did not significantly change the colloidal size (150 nm), the surface charge (-65 mV) and the dispersity (0.1) (Fig. 1B). Additionally, the NP morphology observed by transmission electron microscopy was also unchanged (Fig. S1). For the drug loading, the encapsulation efficiency of $Pam_3CSK_4$ was 100%, as previously described by the authors (Lamrayah et al., 2019), for a 90% adsorption efficiency of dPreS1 (passively measured by the absorbance of the unbound peptide, unshown data). The weights ratio of $Pam_3CSK_4$, dPreS1 and PLA in the final formulation was fixed at 0.12:1:30.

A

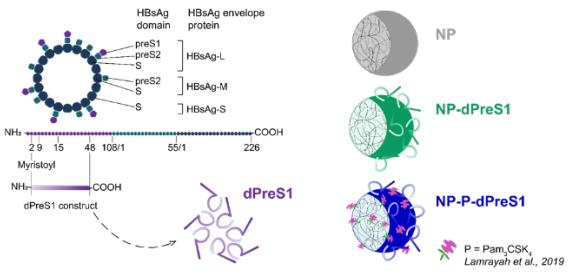


B

| | Size (nm) | PDI | Zeta potential (mV) | Drug loading |
|---|---|---|---|---|
| NP | 150 | 0.102 | -62 | P = $Pam_3CSK_4$ = 120 µg/mL |
| NP-dPreS1 | 150 | 0.102 | -62 | dPreS1 = 1000 µg/mL |
| NP-P-dPreS1 | 150 | 0.108 | -65 | PLA = 30 mg/mL |
| | | | | $8.71 \times 10^{10}$ NP/mL |

C

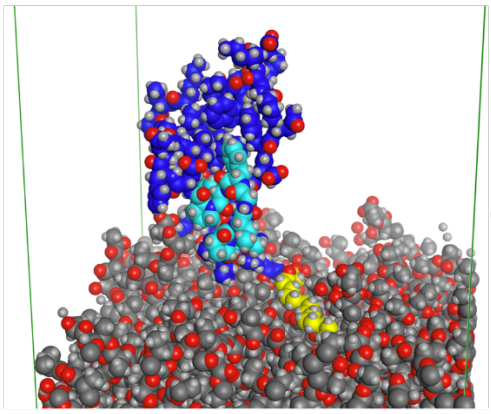

**Fig. 1. NP formulations synthesis was validated and molecular dynamics confirmed the absence of interaction between vectorized dPreS1 and TLR2 agonist. (A)** dPreS1 construct (2-48 AA with N-ter myristoylation) is derived from the HBsAg-L surface protein. **(B)** Standard colloidal properties of formulations (size, PDI and surface charge) were verified in order to control the homogeneity and stability. **(C)** Picture extracted from video S1 at the end of the dPreS1-PLA surface interaction simulation showing that the biologically relevant epitope of dPreS1 (9-15 AA sequence, showed in cyan) has a stable conformation and is totally accessible for intermolecular interactions after the adsorption. The lipidic anchor is in yellow, the rest of the peptide in dark blue, PLA chains in dark grey, red and light grey for carbon, oxygen, and hydrogen atoms respectively. The boundaries of the periodic cell are highlighted in dark green. *PDI = polydispersity index.*

The PreS1 domain of HBsAg (Fig. 1A) is known to specifically bind to the NTCP receptor located at the basolateral side of hepatocytes, allowing the viral entry to the cell. More precisely, both the myristoylated tail (on glycine residue at position 2) and the highly conserved motif 9-NPLGFFP-15 are crucial for receptor binding and infectivity (Glebe et al., 2005). The behavior of the dPreS1 peptide onto the surface of the PLA NP was thus investigated by performing Molecular Dynamics (MD) simulations. Previously published molecular modeling studies evidenced the major role of fatty acid chains for the interaction of biological molecules with PLA NP (Lamrayah et al., 2019; Megy et al., 2020). Consequently, the MD was initiated with the lipidic anchor of dPreS1 (myristic acid) directly facing the PLA surface. After a preliminary equilibration phase, a 200 ns molecular simulation was performed. As illustrated in the video (Video S1), the biologically relevant epitope (9-15 NPLGFFP, in cyan) was not entirely accessible for intermolecular interactions at first, and progressively undergone several adjustments in its conformation, leading to an improved accessibility of the relevant epitope after 100 ns of simulation time. The simulation showed the binding process is possible, and the interaction between dPreS1 and PLA NP evidenced the stabilization of the epitope in an accessible and opened conformation (Fig. 1C). Noteworthy, the lipidic anchor stayed in close contact with the PLA chains during the complete simulation without penetrating the layer, and both their respective conformations were slightly modified, suggesting hydrophobic interactions. Previous findings demonstrated that the three palmitic chains of $Pam_3CSK_4$ are buried into PLA surface, limiting hindrance of both lipidic parts in the final formulation (Lamrayah et al., 2019). Concerning both peptidic parts, the absence of interactions which could lead to unexpected results in terms of epitope stability or accessibility had to be verified. In this regard, docking experiments were performed between the CSKKKK peptidic part of $Pam_3CSK_4$ and the 47 AA sequence of dPres1. All the results exhibited high positive scores, with a top ten average reweighted score of 60.1 Rosetta Energy Units, demonstrating that there is absolutely no possible

interaction between the peptides of the respective molecules (data not shown). As a result, dPreS1 and $Pam_3CSK_4$ did not interact in our system and thus, neither the structure nor the stability of the dPreS1 epitope could be affected by the presence of $Pam_3CSK_4$. Thus, the chemical stability of the NP-P-dPreS1 formulation was validated and results confirm that the relevant epitope (9-15 NPLGFFP) is unchanged and available for recognition by the lymphatic system.

### 3.2. PLA NP efficiently accumulates in the draining lymph nodes and the TLR adjuvant influences the kinetics of germinal center formation

The importance of germinal center (GC) formation for generating a high-quality and robust Ab response is largely highlighted in the literature (Arulraj et al., 2019; Victora and Nussenzweig, 2012). Here, since the antiviral strategy is based on the induction of a strong neutralizing Ab response, it appears essential to explore the early uptake of the formulations following subcutaneous (s.c) administration as well as the subsequent effects in the secondary lymphoid organs (*i.e.* LN). Recent studies have demonstrated the ability of nanovectors to reach the LN after s.c injections (Havenar-Daughton et al., 2019; Singh, 2021). Precisely, NP with a diameter of 100 nm and more are entrapped at the injection site by peripheral DCs available in the local interstitial matrix and carried to LN for B cell presentation (Schudel et al., 2019). Thus, the lymphatic biodistribution after s.c administration of the PLA nanovaccines was monitored, and the GC formation, underlying the immune activation within the draining LNs (dLN), was assessed.

For this, the biodistribution profile of fluorescent PLA NP vectorizing the near infrared DiR probe was investigated using a whole-body 3D fluorescence tomography. These fluorescent NP(DiR) are similar to the active nanovaccine candidates NP(DiR)-dPreS1 in terms of physicochemical characteristics (Fig. S2A) and in the elimination kinetic profile (Fig. S2B and S2C). SKH1 mice were monitored for seven days after a unique s.c injection in the neck region and the detected fluorescence was quantified at 2, 24 hours and 7 days post injection. Noteworthy, the choice of both a hairless strain and a near infrared probe prevented the bias of autofluorescence. A whole-body observation following two axes (dorsal and sagittal) revealed an efficient diffusion and accumulation of the NP to the dLN (Fig. 2). More specifically, these data showed the PLA nanoplatform yields a prolonged and diffused uptake through the lymphatic system, reaching the dLN from 2 hours onwards. The analysis 7 days post immunization also highlighted the persisting biokinetic profile of the NP at the injection site as well as the greater diffusion to non-dLN.

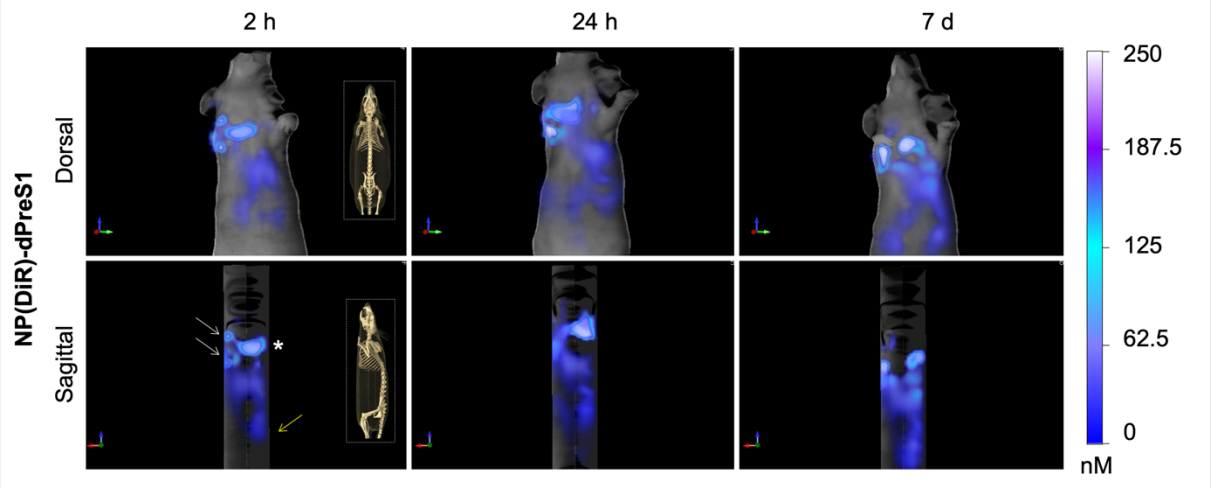


**Fig. 2. Biodistribution profile of the fluorescent NP-dPreS1 following subcutaneous administration shows prolonged retention time and diffusion.** A single s.c injection (neck region, the injection site is shown by the asterisk) was performed on SKH1 female mice with fluorescent NP(DiR)-dPreS1. The fluorescence intensity (750/780 nm) was monitored for 7 days

using FMT imaging (Fluorescence Molecular Tomography, FMT4000, Perkin Elmer). Two observation axes were imaged to prove the high penetration score of the fluorescent PLA NP after s.c administration: through the lymphatic system, PLA NP can reach the proximal (white arrows) and distal (yellow arrow) LN.

The first immunization in a protein prime-boost regimen is critical for the subsequent unfolding of the immune response. To confirm the nanovaccine draining uptake and validate the immune activation in LN, CB6F1 mice were immunized once subcutaneously with NP-dPreS1 or NP-P-dPres1 formulations and LN were harvested at predetermined time points for histological analyses (Fig. 3A). NP and soluble dPreS1 injections were both used in control groups. Classically, the GC formation kinetic is described as fully established 7 days after immunization by a soluble Ag (De Silva and Klein, 2015), but considering the prolonged retention effect of nanoparticulate formulations, three mice per group were euthanized at days 14, 21 and 28 post-immunization for a more precise understanding of the biokinetics. The draining inguinal LNs were stained to identify the follicular B cells (using IgD Ab) and the mature GCs (using peanut agglutinin (PNA)). NP-dPreS1 showed a GC response at day 21 post-immunization (Fig. 3B) which decreased at day 28 when in parallel it appeared for NP-P-dPreS1 (Fig. 3C).

To understand this delay, the B-cell-recruiting factor CXC chemokine ligand 13 (CXCL13) expression was monitored in mice serum. This chemokine plays an important role in B cell follicle migration (Havenar-Daughton et al., 2016). Serum levels of CXCL13 increased at day 14 only for NP-P-dPreS1 (Fig. 3D).

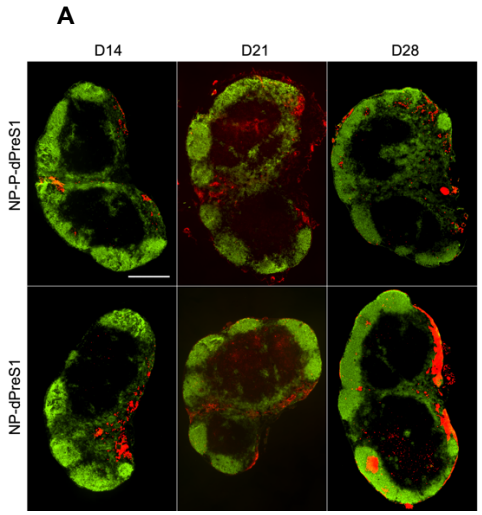

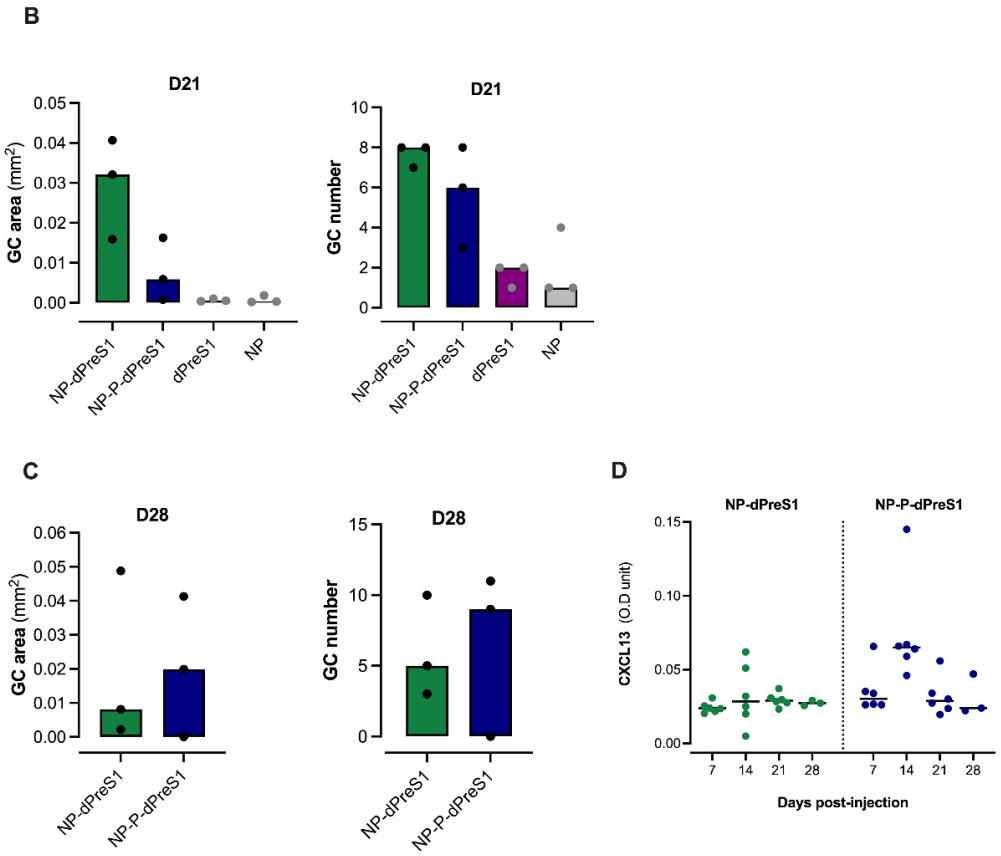


**Fig. 3. Draining lymph node responses after a unique s.c administration reveals distinct GC kinetics and numbers**. **(A)** Microscopic observation of GC formation over time. LN were harvested and some cryosections were stained with anti-IgD for follicular B cells (*green*) and PNA for GCs (*red*). Scale bar = 500 µm. **(B)** Analyses and number of GC area 21 days after immunization. **(C)** Analyses and number of GC area 28 days after immunization, only for nanovaccines (NP-dPreS1 and NP-P-dPreS1). **(D)** Blood levels of CXCL13 monitored during 28 days.

### 3.3. Nanovaccines provides a long-lasting and strong humoral response in naïve mice

Next, to assess the ability of the nanovaccines to induce a specific anti-dPreS1 response, an immunization assay with naïve mice following a prime boost regimen was performed and the serum IgG titers were longitudinally investigated over one year. CB6F1 female mice were randomly distributed (n=6 per group) and were subcutaneously immunized three times each three weeks as described in Methods and in Fig. 4A. NP-dPreS1 and NP-P-dPreS1 nanovaccine candidates were compared with soluble dPreS1, KLH-dPreS1 (as positive immunogenic control) and NP (as vector control) (Fig. 4B).

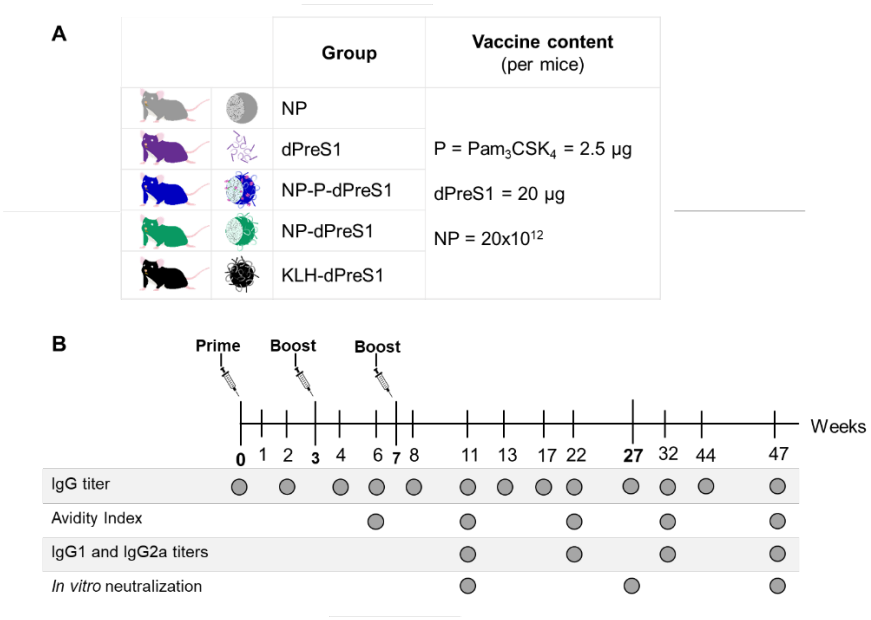


**Fig. 4**. **Detailed study design. (A)** Five experimental treatments were formulated and immunologically evaluated on naive CB6F1 mice. At times of injection, all formulations had equivalent quantities of NP ($20.10^{12}$/mouse), $Pam_3CSK_4$ (2.5 µg/mouse) and dPreS1 (20 µg/mouse). NP and KLH-dPreS1 conditions respectively represent negative and positive controls. **(B)** Mice were kept in experiment during 47 weeks with regular blood analyses to investigate the immune responses after NP-based formulation injections. The following immune parameters were monitored: total anti-dPreS1 IgG, IgG1 and IgG2a titers, Ab avidity, *in vitro* HBV neutralization efficacy of the antisera. At W27, a final heterologous s.c boost was performed: all mice received the NP-dPreS1 formulation (yellow boost) except for the control groups (KLH-dPreS1 and NP) which received their own formulations. Mice were euthanized at W47 using cervical dislocation.

The NP-dPreS1 formulation rapidly elicited elevated titers of anti-dPreS1 IgG reaching about $10^7$ during the plateau phase and remaining still high ($10^6$) after six months with insignificant difference compared to the positive immunogenic control KLH-dPreS1 (Fig. 5). Soluble dPreS1 was immunologically recognized, which is in accordance with the literature (Bian et al., 2017), but still elicited significantly lower quantities of anti-dPreS1 IgG titers reaching $10^5$ during the plateau phase to decrease by one log six months later. Noteworthy, only 50% of the subjects (3/6) responded to immunization in this group (Fig. S5). The addition of $Pam_3CSK_4$ as an adjuvant in NP forms decreased by two log the induced specific IgG quantities, overlapping the IgG profile of the dPreS1 group.

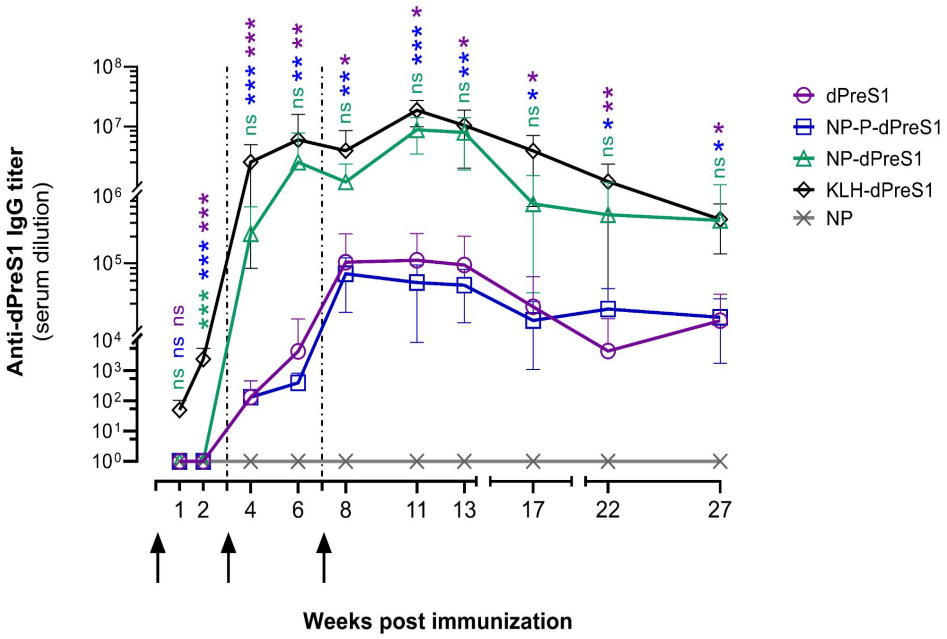


**Fig. 5**. **For each group, anti-dPreS1 IgG titer was analyzed on mice sera from W1 post immunization onwards**. A dPreS1 specific in-house ELISA (limit of detection = 0.01 µg/mL, see Fig. S3) was developed. Each symbol represents an individual animal and full bars indicate the mean of the group for each timepoint. Statistical analysis was performed by ANOVA test with multiple comparisons and Dunnett's correction using positive control KLH-dPreS1 condition as reference. *alpha=0.05, *p<0.05, **p<0.005, ***p<0.001, ns = not significant*.

To qualitatively describe the immune responses, the avidity and isotype of induced IgGs were evaluated. The avidity index represents the total binding strength of the Ag-Ab interaction and can vary during the immune response depending on the affinity maturation and clonal selection processes. Indexes were measured by the ability of the mice antisera to remain in binding with dPreS1 in the presence of 8M urea as detergent (Badamchi-Zadeh et al., 2016). All formulations had low mean avidity indexes after the first immunization, except for KLH-dPreS1 group which showed an intermediate mean index, unchanged until W22. Since KLH is described as strongly immunogenic due to its high molecular mass, the constant intermediate avidity level is not surprising (Harris and Markl, 1999; Swaminathan et al., 2014). In contrast, the Ab avidity increased progressively with time and reached an intermediate mean index for both NP-dPreS1 (31%) and NP-P-dPreS1 (42%) at W22. Interestingly, when considering results individually, NP-dPreS1 formulation induced the most homogenous response at W22 (5/6 mice over 30%) compared to NP-P-dPreS1 which offered the highest response (3/6 mice over 50%). Soluble dPreS1 induced Ab with low or none average avidity (Fig. 6A). Further characterization indicates the Th1/Th2 skewing of the immune response via IgG1/IgG2a titer quantification. IgG1 isotype was predominant for all groups, suggesting a major Th2 cell polarization for all vaccine regimens (Bretscher, 2019) (Fig. 6B).

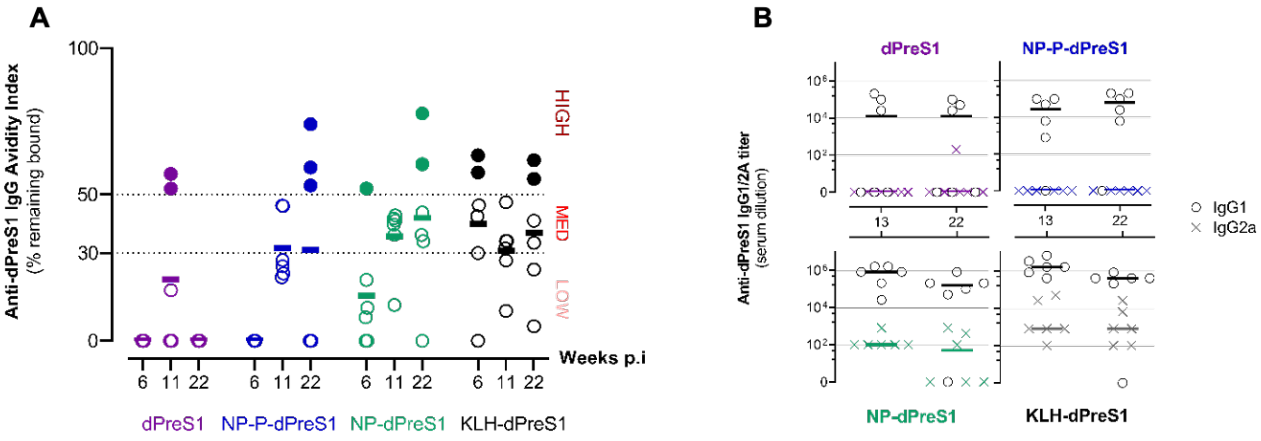


**Fig. 6. Antibody response characterization. (A) Avidity indexes of anti-dPreS1 IgG were measured in mice sera at W6, W11, and W22.** Antisera with index values exceeding 50% were attributed a high avidity, those with index values of 30% to 50% were attributed intermediate avidity, and those below to 30% were attributed a low avidity. Each symbol represents an individual animal and full bars indicate the mean of the group for each timepoint. **(B) IgG1 and IgG2a subtype titers were monitored in mice W13 and W22 sera.** Data are expressed in individual points with bars representing mean.

### 3.4. TLR2 agonist in the nanosystem generates strong neutralizing Ab

The *in vitro* neutralizing efficiency of the anti-dPreS1 Ab was investigated using infected differentiated HepaRG (dHepaRG) (Marion et al., 2010) and HBeAg was quantified as a parameter of viral infection establishment. While W11 sera from soluble dPreS1 immunization showed a weak neutralization effect (75% of HBeAg at 1/100 dilution), other groups induced strong neutralizing Ab against HBV, in a concentration-dependent manner (25%, 24% and 3% of HBeAg for respectively NP-P-dPreS1, NP-dPreS1 and KLH-dPreS1 at 1/100 dilution) (Fig. 7). W27 antisera was investigated similarly and HBV neutralization effect globally decreased (47%, 51% and 7% respectively for NP-P-dPreS1, NP-dPreS1 and KLH-dPreS1 groups). Immunization by soluble dPreS1 did not show any neutralization at W27, echoing the results from W11 (Fig. S5).

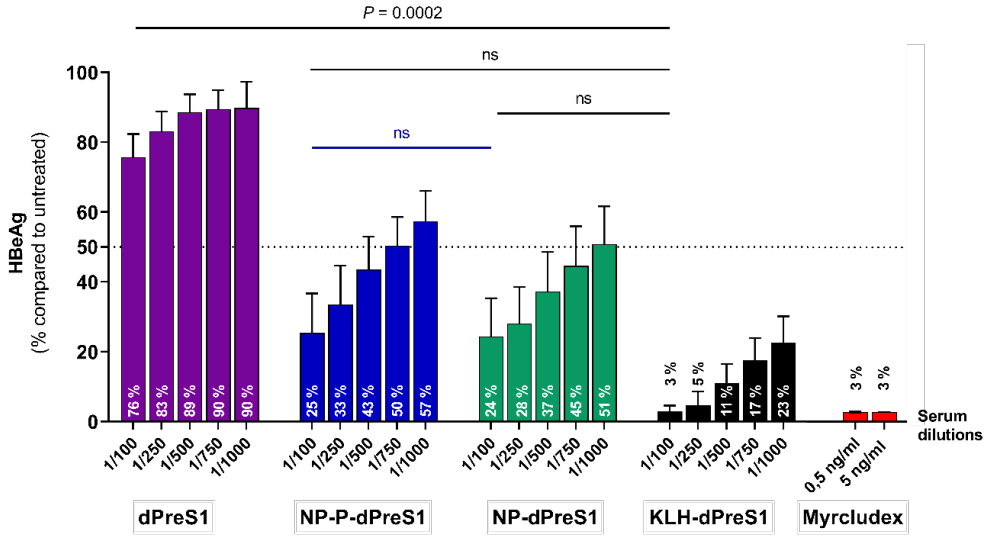


**Fig. 7. *In vitro* HBV neutralization assay by murine anti-dPreS1 IgG from W11.** Serum from W11 were serially diluted and incubated simultaneously with HBV on dHepaRG cell cultures (n=4),

washed the day after and then HBeAg concentrations were measured by ELISA after 7 days. Myrcludex, a polypeptide with HBV entry inhibitory properties, was use as positive control. Data is expressed as the percentage of HBeAg compared to non-treated (mean (SEM)). Two-way ANOVA was used for group comparisons (at 1/100 condition), with Dunnett's multiple comparison *post hoc* test for analysis of specific differences using either KLH-dPreS1 (black bars) or NP-dPreS1 (blue bar) as reference condition. *alpha=0.05*.

Surprisingly, the correlation of neutralizing data to the corresponding IgG titers suggests that $Pam_3CSK_4$ provides a distinct adjuvant-like effect to the immune response. At both W11 and 27, IgG from adjuvanted group showed a comparable neutralization profile as NP-dPreS1 IgG with 100-fold lower Ab level (4/6 mice in the red squared area) (Fig. 8).

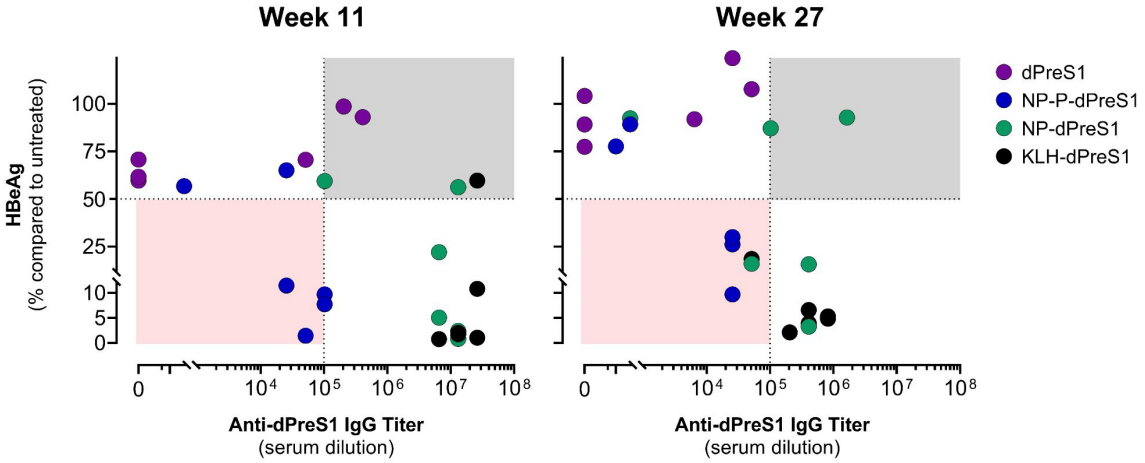


**Fig. 8. $Pam_3CSK_4$ modulates the interactions between NP-dPreS1 and the immune system leading to IgG with the strongest neutralizing activity.** For each murine serum at W11 and 27, HBV neutralization activity (y axis) is represented according to the corresponding anti-dPreS1 IgG titer (x axis). Red squared areas highlight conditions with high neutralization power and low IgG titer, the most efficient combination. In contrast, gray squared areas highlight conditions with low neutralization power and high IgG titer. Data was gathered separately for easier visualization and each point represents one subject.

### 3.5. Late heterologous boost confirms the essential role of nanovectorization for immune benefit

The effect of a heterologous boost at W27 using the NP-dPreS1 candidate was investigated on NP-dPreS1 and NP-P-dPreS1 groups. Both received a s.c injection of NP-dPreS1 while control groups (KLH-dPreS1 and NP) received their respective formulations. The rational was based on the literature suggesting that heterologous prime-boost can be more immunogenic than simple homologous strategy (Kardani et al., 2016; Lu, 2009). Concerning the soluble dPreS1 prime/NP-dPreS1 boost group (*purple data*), IgG titer and avidity index strongly increased without any effect in neutralization activity, confirming the crucial role of the prime immunization (Fig. 9A) (Havenar-Daughton et al., 2019). For the NP-P-dPreS1 prime/NP-dPreS1 boost group (*blue data*), we observed a similar increase of IgG titer and avidity index (Fig. 9B) with, more interestingly, a Th1 cell polarization is induced with the emergence of IgG2a at W32 (Fig. 9D). The neutralization activity of these Ab is also greatly impacted with two-fold lower of HBeAg % level (from 46.5% at W27 to 23.5% at W47). Regarding NP-dPreS1 (*green data*) and KLH-dPreS1 (*black data*), they received their own homologous boost (to maintain the thoroughness of the controls), consolidating the strong existing immune response with highest avidity indexes changing from both medium to high levels. The neutralization level is higher for NP-dPreS1 (from 51.2% to 33.0%), while it is

unchanged for KLH-PreS1. Similar to the conventional prime-boost-boost regimen, NP-P-dPreS1 group showed high neutralization efficiency while IgG titer is the lowest (*blue dots*), with 5/6 mice in the most efficient area (Fig. 9C).

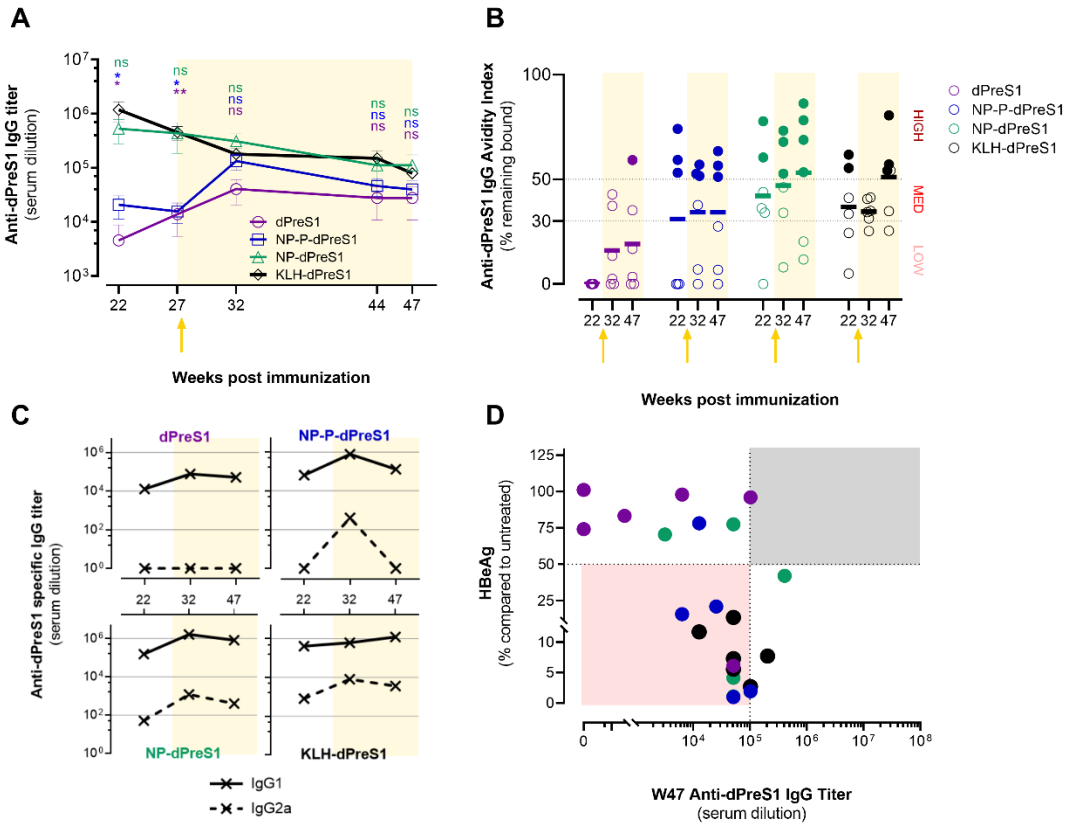


**Fig. 9. NP-dPreS1 s.c boost immunization on W27 improves the IgG titer and the neutralization effect (A)** Anti-dPreS1 IgG profiles from W22 to 47 with increase of titers for dPreS1 and NP-P-dPreS1 formulations following final heterologous boost (*yellow arrow*). Data is expressed as mean (SD) and statistical analysis was performed by ANOVA test with multiple comparisons and Dunnett's correction using positive control KLH-dPreS1 condition as reference. *alpha=0.05, *p<0.05, **p<0.005, ***p<0.001.* **(B)** Avidity Index (%) after the final W27 boost also increases for all conditions. Full bars represent the mean for each condition. **(C)** Interestingly, IgG2a titers increase for nanoparticulate formulations (*blue and green*) but not for soluble dPreS1 (*purple*), following the final heterologous boost. **(D)** Neutralization effect compared to specific IgG titer at W47 hints at the added value of using a TLR adjuvant in therapy.

Concerning the toxicity profile of nanoformulations, the body weight of the mice was regularly monitored as well as the liver and spleen weights at the endpoint. Any general toxicity regarding these weights couldn't be detectable (Fig. S6). Further studies are intended to precisely describe the toxicological aspect, precisely the immunological consequence of a such treatment.

## 4. Discussion

In 2016, the World Health Organization stated the HBV elimination for 2030 as a global public health aim, by notably increasing the vaccine coverage from 82% to 90%. The development of novel vaccine technologies is thus crucial to reach it seeing as the current vaccine is sub-optimal (Block et al., 2021; Dolgin, 2022). Here, we have investigated the combination of a multivalent nanoplatform for an optimized Ag presentation with a TLR ligand entrapped in the delivery system to strengthen the neutralizing immune response. First, the nanosystem platform (PLA NP) is

synthesized by nanoprecipitation, an easy-to-use and industrially transposable process which enables the production of reproducible and stable formulations. Second, an optimized antigenic peptide, already used in clinical settings and derived from HBsAg, was adsorbed at the surface of the NP. Lastly, since the induction of a strong and durable Ab response to vaccination is highly dependent on the use of effective adjuvants that stimulates the innate immune system (Pulendran and Ahmed, 2011), we chose to vectorize a TLR 1/2 agonist, $Pam_3CSK_4$ entrapped in the PLA NP core to potentiate the immunization process.

In the first part of this study, straightforward molecular modeling results show that the choice of $Pam_3CSK_4$ as the adjuvant and dPreS1 as the protein Ag is highly relevant in terms of chemical mechanics. Indeed, both molecules do not interact with each other when formulated within the NP. More precisely, vectorizing the antigen should be able to expose the dPreS1 epitopes, in presence or not of $Pam_3CSK_4$, with no structural modification, and subsequently trigger identical conformational Ab responses. This delivery system elegantly increases the immunogenicity and stability of the Ag, by gathering it in nano-scale clusters and decreasing its risks of degradation. Next, via crossed bioimaging and histological evaluations, we documented that an efficient entry of vaccine into the lymphatic vessels can lead to an immune response by favoring the right timing and right location in dLN. The biodistribution profile of fluorescent PLA nanosystems in mice show a long-term stay in the secondary lymphoid organs, which is in favor of a slow and localized delivery of the Ag. Interestingly, the adsorption of dPreS1 on the NP generates higher accumulation of the vaccine in the draining areas but also facilitates the transport across tissues, leading to a greater spatial diffusion over time. These data demonstrate that NP formulations have appropriate colloidal and surface properties required for the dynamic process of immunization (Kelly et al., 2019).

Next, and despite initial delays in B cell activation and GC formation compared to controls, we showed that the anti-PreS1 IgG titers and avidity indexes reached higher levels for the dually functionalized formulation (NP-P-dPreS1). It is worth noting that both these read outs emphasize the advantage of the nanovectorization on the bioavailability of the antigen and/or TLR1/2 adjuvant, based on the intragroup response heterogeneity for the soluble dPreS1 compared to the NP groups (Fig. S4). The increase in titers and avidity is in accordance with the general (Pedersen et al., 2020) and the TLR-specific (DeFranco et al., 2012) literature, explaining the simultaneous but delayed stimulation of both BCR and TLR signaling pathways. These findings also corroborates with past papers indicating that activation of the TLR2-mediated NF-κB pathway in GC B cells controls GC maintenance and differentiation (Heise et al., 2014). Desmares *et al* recently confirmed $Pam_3CSK_4$ specifically induced the activation of this canonical NF-kB pathway (Desmares et al., 2022). Noteworthy, control groups (soluble Ag and NP) activated B cells after being taken in charge by Ag-presenting cells but induced less GC formation and less or no IgG production. In parallel, we report an elevation of serum CXCL13 levels during early immunization in presence of $Pam_3CSK_4$, explained by the fact that CXCL13 expression occurred as a consequence of NF-κB activation (Kazanietz et al., 2019). Altogether, these data are in favor of an enhanced spatiotemporal access of the antigen and the adjuvant via their vectorization by the PLA NP.

Subsequently, we confirmed the higher neutralizing capacity of vaccine-specific IgG when the Ag is loaded onto NP versus the soluble form. Here again, in absence of a delivery system, the soluble dPreS1 protein is rapidly exposed to proteolytic enzymes after subcutaneous administration which impeded its presentation to the immune system (Varkhede et al., 2020). This observation validates the previously established belief that drug drivers (Collins et al., 2017), such as NP (Kelly et al., 2019), act as an efficient carrier for Ag transit, protection from the environment and presentation to the lymphatic system. Likewise, vectorized dPreS1 is delivered to the LN for recognition and internalization in higher-concentrated clusters, enhancing its immunogenicity (Kasturi et al., 2011).

Although there is no direct experimental explanation for this phenomenon yet, together with the MD data these findings prompted us to hypothesize that the doubly-functionalized NP has a synergistic effect between the adjuvant and the Ag and that the quality of the Ab prevails over their quantity. Future experiments are ongoing to verify this assumption.

The neutralization data also show evidence of direct HBV entry inhibition in dHepaRG cells, indicating the Ab are effective at recognizing the 9-15 AA sequence of the viral surface protein and obstructing the PreS1/NTCP interaction (Urban et al., 2014). This observation reveals the diversity of B cell Ab-response to dPreS1 Ag in terms of immunoglobulin repertoire and neutralizing activity depending on the vaccine candidate. Next, we prove the added value of $Pam_3CSK_4$ adjuvant properties since mice immunized with NP entrapping this molecule led to greater humoral immune responses with higher virus-neutralizing Abs compared to NP formulated with dPreS1 only. The TLR1/2 ligand reinforces the quality of the immune response via the upregulation of proinflammatory genes subsequently leading to cytokine production and early B cell maturation improvement. Overall, NP-P-dPreS1 vaccine illustrates relevant preventive immunization properties. Again, after the heterologous boost, the presence of the adjuvant elicited the most interesting neutralizing activity of induced Ab with the highest neutralization efficiency adjusted to the IgG titers, and sustainable all over the year.

We have summarized in Fig. 10 the current hypothesis regarding the immune key components responsible for triggering such optimal immune response when combining an adjuvant and a vaccine antigen onto the same polymeric particle. As one of the major challenges in vaccinology these days is to pin point which critical parameters of the innate immunity participates in the programming of the adaptive response, additional analyses of immune responses should be further characterized for full appreciation of the mechanism involved when using such nanoformulations. Typically, the enhanced quality of Ag produced could be studied by cloning and sequencing of B cell to identify Ab sequence with improved neutralizing properties.

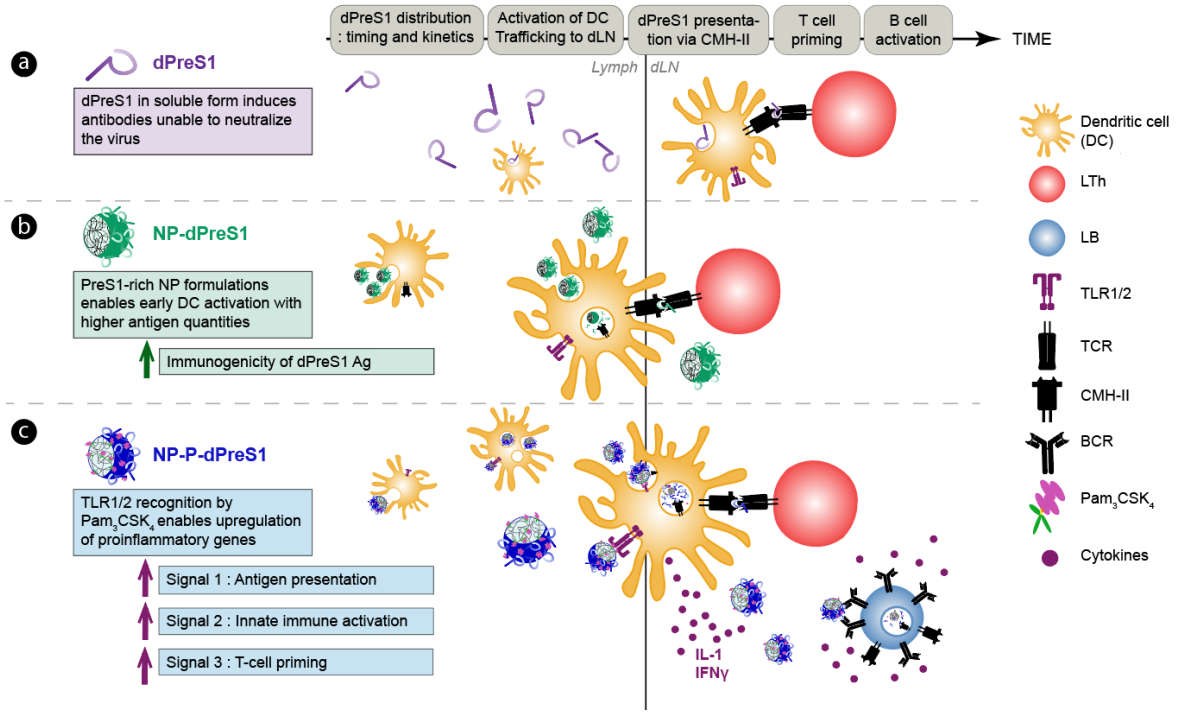


**Fig. 10. Nanoadvantages and suggested immune mechanism triggered by soluble dPreS1 versus adjuvanted or not NP-dPreS1 formulations. (a)** Poor bioavailability of free-form soluble dPreS1 translates into suboptimal Ab production with late activation in dLNs of the immune cells.

**(b)** LN trafficking and Ag immunogenicity: Nanovectorization gives rise to high-concentrated clusters of dPreS1 Ag able to traffic longer in the lymphatics, two parameters that may explain an enhanced immunogenicity of the Ag. **(c)** Innate immunity boost: TLR2 stimulus by $Pam_3CSK_4$ may synergize with dPreS1 response and improve the GC pathway of memory B cell formation via three different signals namely the enhancement of (i) the Ag presentation by DC, (ii) the innate immune pro-inflammatory cytokines, and (iii) the subsequent T cell priming of HBV-specific CD4+ and CD8+. In fact, the affinity selection of GC B cells is dependent on T cells (Pulendran, 2009).

Altogether, these results give high hopes for developing a successful therapeutic solution against chronic HBV infections. Abundant efforts have been made to develop therapeutic vaccines but most candidates have missed their primary endpoints, which may be attributed to the fact that they have been composed of free Ag or micro-delivery systems, contributing to low uptake in the lymphatics and failure to induce optimal protection (Kosinska et al., 2017; Li et al., 2017). With the recent exception of two elegant studies, nearly no nanosystem solution has been explored (Qiao et al., 2021; Wang et al., 2020). Qiao and colleagues propose a nanosystem based on chitosan and heparin while Wang and colleagues developed a system based on ferritin NP. In terms of biomaterials, chitosan is known to be very expensive and hard to produce in a reproducible manner, while ferritin is a metallic-based system, which is less biocompatible and biodegradable than PLA (Bellich et al., 2016). Nonetheless, mirroring our results, both these nanosystems display excellent lymph node targeting following subcutaneous injections, as well as high IgG titers ($10^7$ $\log_{10}$ at week 7). Our novel subcutaneous delivery system could be part of the next generation antiviral treatments for hepatitis patients, considering the long-lasting and highly specific immune protection it triggers against PreS1 epitope. Strong tolerance to HBsAg have been shown to limit the therapeutic effect of conventional vaccinations in both preclinical models and patients with chronic hepatitis B infections. In the latter, immune tolerance to PreS1, if any, appears to be much lower than that to HBsAg, as it is only secreted in trace amounts compared to HBsAg that is present in a $10^2$-fold to $10^5$-fold excess over virions (Durantel and Zoulim, 2016). Now, the formulation needs to be challenged *in vivo* against HBV. This working hypothesis in AAV-HBV transduced mice is currently undergoing. Such platforms are easily tunable and could quickly be adapted to any viral genotype if the corresponding antigen is carefully selected. We could also imagine delivering both the adjuvant and the Ag in separate PLA NP, offering flexibility in coupling a generic adjuvant-containing NP with a novel antigen-containing NP (Boyoglu-Barnum et al., 2021; Singh et al., 2007). Other nanoplatforms can also be envisaged such as polymeric micelles already proved as efficient adjuvants for vaccine delivery (Lamrayah et al., 2022).

Taking an even bigger step back, the precise characterization of this nanosystem participates in broadening the R&D opportunities for hard-to-get microbes, such as HIV, *Plasmodium falciparum*, or *Mycobacterium tuberculosis*. Incorporating such PLA NP in delivery systems like microneedle platforms or hydrogels for high-mucus penetration would enable a better protection, with a mucosal-specific immune activation at the localized site of entry of these pathogen (Du et al., 2022; Lavelle and Ward, 2022).

## Conflict of interest

All authors declare no conflict in interest except B.V. who holds some shares in Adjuvatis. The company had no role in the design of the study; in the collection, analyses, or interpretation of data; in the writing of the manuscript or in the decision to publish the results. The other authors declare no conflict of interest.

## Authors contributions

B.V., J.L. and D.D. conceived the idea, designed and supervised the work. M.L. and F.C. wrote the original manuscript. S.M. and R.T. performed all in silico experiments. C.C., M.D. and D.D. performed all in vitro experiments. E.C. performed all ex vivo experiments. M.L. and F.C. performed all in vivo experiments. All authors have read, revised and agreed to the published version of the manuscript.

## Acknowledgements

The authors would like to thank the staff of AniCan platform (CRCL, Lyon) and Thomas Barré for his assistance in FMT4000 equipment, PHENOCAN for imaging devices [grant number ANR-11-EQPX-0035 PHENOCAN], all the staff of Plateau de Biologie Expérimentale de la Souris (ENS, Lyon) for the generous advice with animal care, CTμ platform (Université Lyon 1) and Altan Yavuz for electron microscopy assistance.

## Financial support

This work was supported by “La Ligue contre le Cancer” to BV and DD and a PhD scholarship to ML. This work was also supported by ANRS-MIE (French research agency on infectious and emerging diseases) to BV and DD (ECTZ 62760 and ECTZ 160315) and through PhD scholarships to FC (ECTZ158412) and MD (ECTZ137751). Global financial supports were also obtained from CNRS and INSERM.

**Supplementary Data**

*Video attached to the manuscript*

**Video S1.** This video highlights the last 20 ns of the 200 ns simulation experiment. The last 1000 frames out of the 10,000 total frames of the dynamic were used. The simulation has reached a stable state as no large molecular motion is observed. The biologically relevant epitope remains accessible for intermolecular interactions throughout the complete capture. The epitope is displayed in cyan, the lipidic anchor in yellow, and the rest of the PreS1 peptide in dark blue. PLA chains are displayed in dark grey, red and light grey for their carbon, oxygen, and hydrogen atoms respectively. The boundaries of the periodic cell are highlighted in dark green.

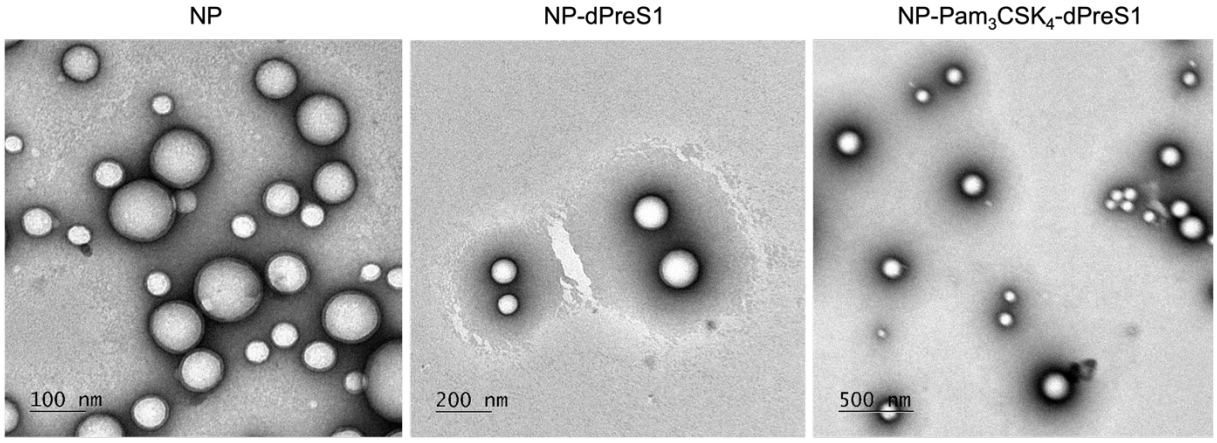


**Fig. S1. Transmission electron microscopy images of blank NP (left), NP-dPreS1 (center) and NP-$Pam_3CSK_4$-dPreS1 (right).** The three types of nanoformulations are morphologically similar (scale bar in each image).

**A**

| | **Size** (nm) | **PDI** | **Zeta potential** (mV) |
|---|---|---|---|
| NP(DiR) | 160 | 0.078 | -61 |
| NP(DiR)-dPreS1 | 162 | 0.090 | -64 |

**B**

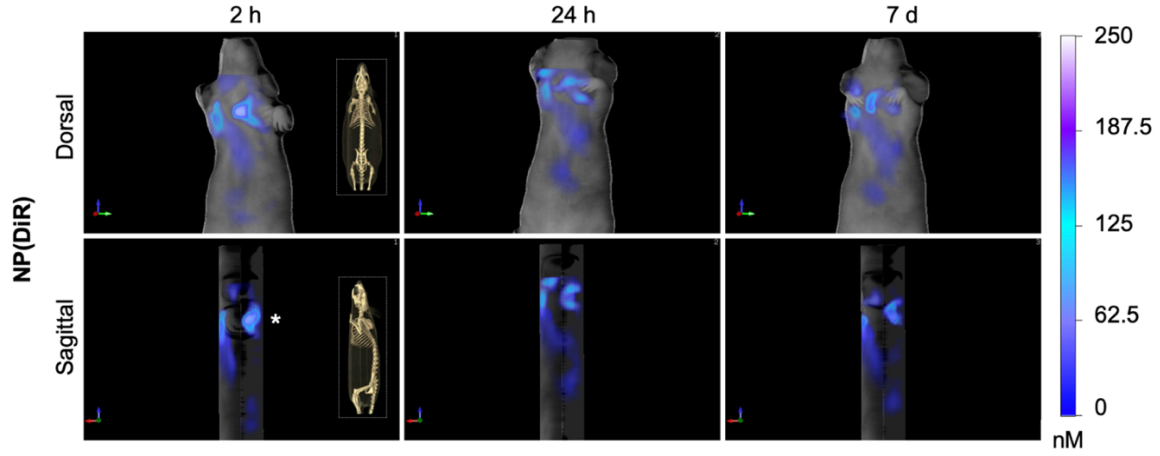


**C**

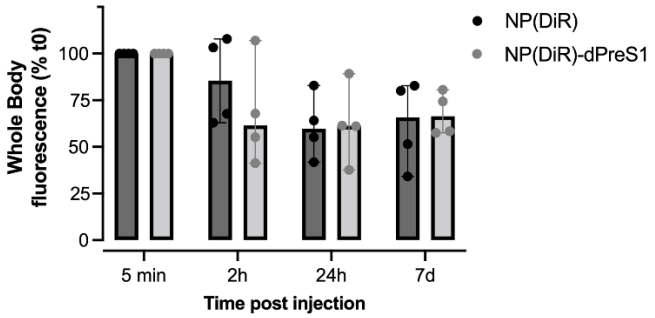


**Fig. S2. Comparative study of the biokinetics of the NP formulations functionalized or not with dPreS1. (A)** Standard colloidal properties of fluorescent formulations (size, PDI and surface charge) containing or not the modified dPreS1 peptide. **(B)** A single s.c injection (neck region, the injection site is shown by the asterisk) was performed on SKH1 female mice with fluorescent NP(DiR). The fluorescence intensity (750/780 nm) was monitored for 7 days using FMT imaging (Fluorescence Molecular Tomography, FMT4000, Perkin Elmer). **(C)** Fluorescence signal quantification measured by FMT in NP(DiR) or NP(DiR)-PreS1 injected mice, at different time points. Each point represents an individual animal and results are expressed as median (95% CI). Statistical differences between the two groups at each time were evaluated using the non-parametric Wilcoxon test. There is no statistical difference between the two fluorescence signals at each time.

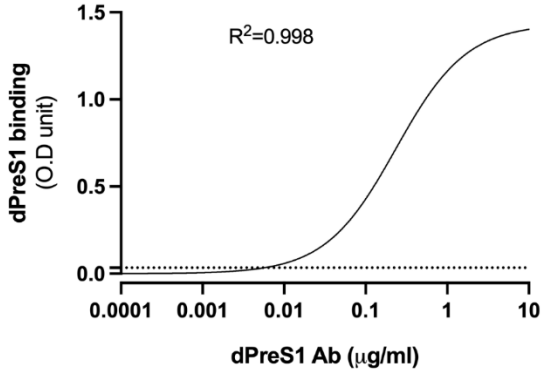


**Fig. S3. In-house sandwich ELISA for quantitative detection of specific dPreS1 Ab.** We have serially diluted a solution of anti-PreS1 Ab in dPreS1-coated plates. The limit of detection (LOD) is defined as LOD = μ blank + 3σ, and is represented by the dotted line.

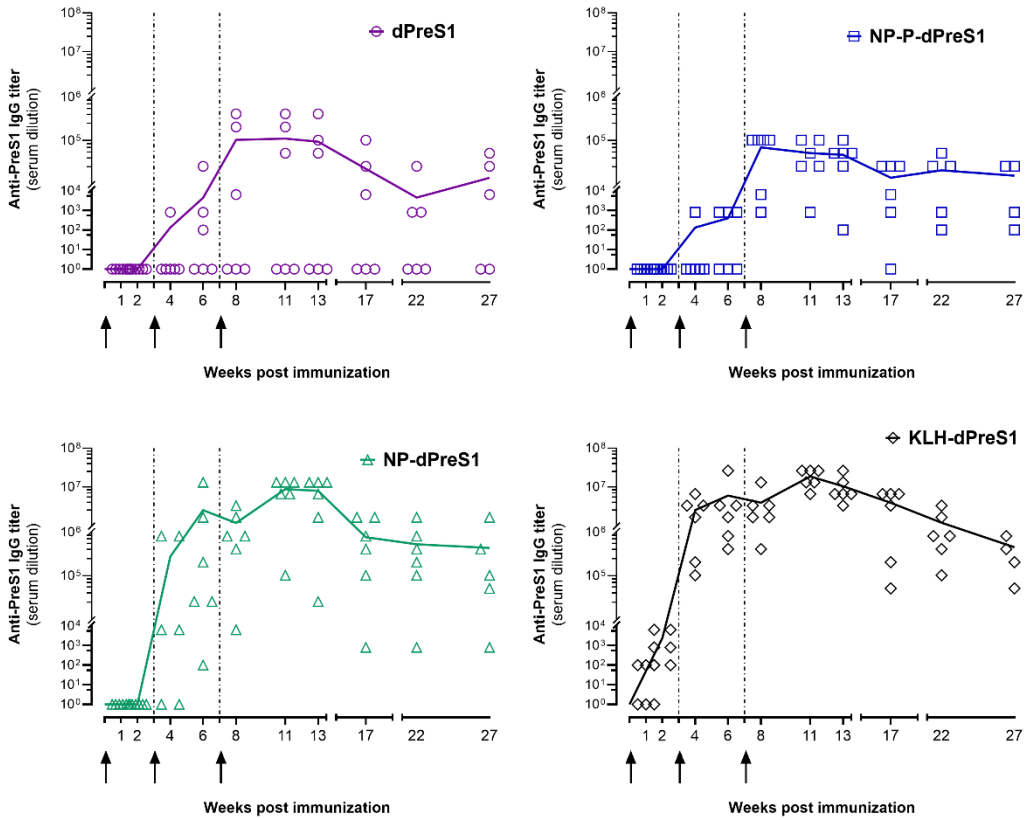


**Fig. S4 IgG anti-dPreS1 titers, schematically represented in individual values.** *See legend of Figure 5*

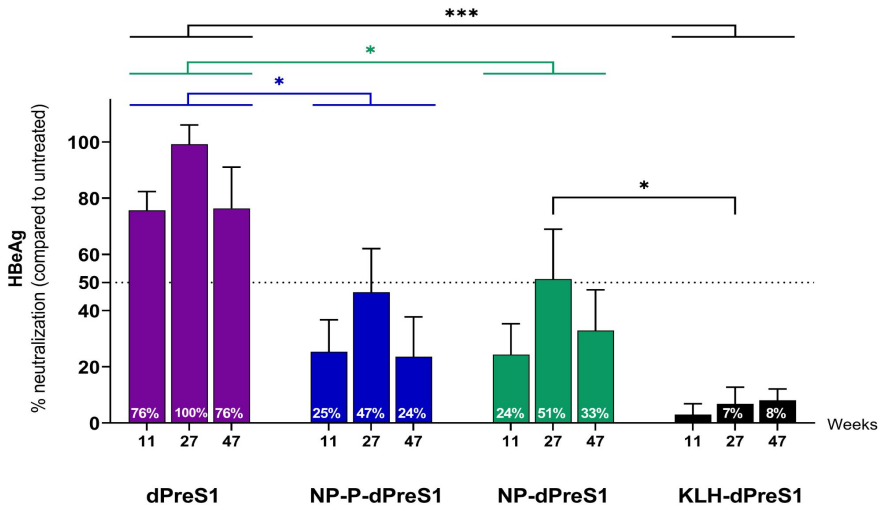


**Fig. S5. Comparative data of the neutralization activity of mice antisera at W11, W27 and W47 in bar charts, at serum dilutions 1:100.** Intragroup statistical analysis was performed by ANOVA test with multiple comparisons and Tukey's correction. For all groups, there was no intra-group difference ($\alpha = 0.05$) between the different time points.

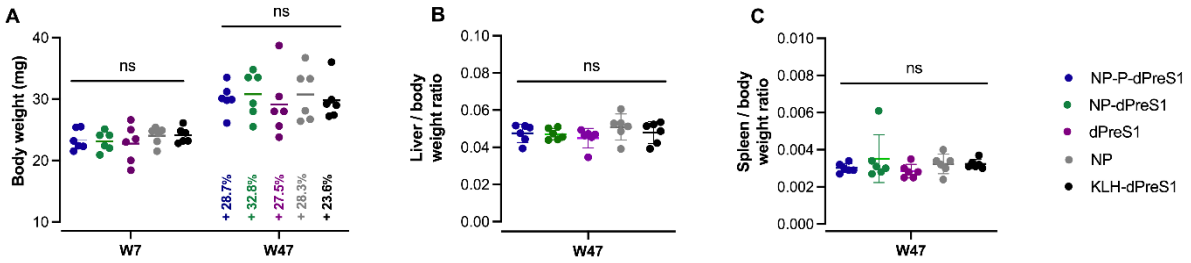


**Fig. S6. General safety evaluation based on weights is in favor of a safe-by-design nanoplatform.** For toxicity surveillance, mice body weights were monitored at W7 and W47 with indicated each evolution rate (A). At endpoint, their liver (B) and spleen (C) were also weighed after cervical dislocation and dissection. Upon evaluation, no statistical difference was observed between groups (ANOVA test for A, Kruskal-Wallis test for B and C). Mice were physiologically heavier at one year old with an increasing weight between + 23.6% and + 32.8% compared to W7 weight. This information is important because toxicity can easily become a serious obstacle in the potential safety of a vaccine, especially when complemented by adjuvants. *ns = non significant.*

## REFERENCES


Anwar, M.A., Shah, M., Kim, J., Choi, S., 2019. Recent clinical trends in Toll-like receptor targeting therapeutics. Med. Res. Rev. 39, 1053–1090. https://doi.org/10.1002/med.21553

Arulraj, T., Binder, S.C., Robert, P.A., Meyer-Hermann, M., 2019. Synchronous Germinal Center Onset Impacts the Efficiency of Antibody Responses. Front. Immunol. 10. https://doi.org/10.3389/fimmu.2019.02116

Badamchi-Zadeh, A., McKay, P.F., Korber, B.T., Barinaga, G., Walters, A.A., Nunes, A., Gomes, J.P., Follmann, F., Tregoning, J.S., Shattock, R.J., 2016. A Multi-Component Prime-Boost Vaccination Regimen with a Consensus MOMP Antigen Enhances Chlamydia trachomatis Clearance. Front. Immunol. 7, 162. https://doi.org/10.3389/fimmu.2016.00162

Bellich, B., D'Agostino, I., Semeraro, S., Gamini, A., Cesàro, A., 2016. "The Good, the Bad and the Ugly" of Chitosans. Mar. Drugs 14, 99. https://doi.org/10.3390/md14050099

Bian, Y., Zhang, Z., Sun, Z., Zhao, J., Zhu, D., Wang, Y., Fu, S., Guo, J., Liu, L., Su, L., Wang, F.-S., Fu, Y.-X., Peng, H., 2017. Vaccines targeting preS1 domain overcome immune tolerance in hepatitis B virus carrier mice. Hepatology 66, 1067–1082. https://doi.org/10.1002/hep.29239

Block, T.M., Chang, K.-M., Guo, J.-T., 2021. Prospects for the Global Elimination of Hepatitis B. Annu. Rev. Virol. 8, 437–458. https://doi.org/10.1146/annurev-virology-091919-062728

Boyoglu-Barnum, S., Ellis, D., Gillespie, R.A., Hutchinson, G.B., Park, Y.-J., Moin, S.M., Acton, O.J., Ravichandran, R., Murphy, M., Pettie, D., Matheson, N., Carter, L., Creanga, A., Watson, M.J., Kephart, S., Ataca, S., Vaile, J.R., Ueda, G., Crank, M.C., Stewart, L., Lee, K.K., Guttman, M., Baker, D., Mascola, J.R., Veesler, D., Graham, B.S., King, N.P., Kanekiyo, M., 2021. Quadrivalent influenza nanoparticle vaccines induce broad protection. Nature 1–6. https://doi.org/10.1038/s41586-021-03365-x

Bray, F., Ferlay, J., Soerjomataram, I., Siegel, R.L., Torre, L.A., Jemal, A., 2018. Global cancer statistics 2018: GLOBOCAN estimates of incidence and mortality worldwide for 36 cancers in 185 countries. CA. Cancer J. Clin. 68, 394–424. https://doi.org/10.3322/caac.21492

Bretscher, P., 2019. On Analyzing How the Th1/Th2 Phenotype of an Immune Response Is Determined: Classical Observations Must Not Be Ignored. Front. Immunol. 10. https://doi.org/10.3389/fimmu.2019.01234

Brisse, M., Vrba, S.M., Kirk, N., Liang, Y., Ly, H., 2020. Emerging Concepts and Technologies in Vaccine Development. Front. Immunol. 11, 583077. https://doi.org/10.3389/fimmu.2020.583077

Chaudhury, S., Gray, J.J., 2008. Conformer Selection and Induced Fit in Flexible Backbone Protein–Protein Docking Using Computational and NMR Ensembles. J. Mol. Biol. 381, 1068–1087. https://doi.org/10.1016/j.jmb.2008.05.042

Cheng, D., Han, B., Zhang, W., Wu, W., 2021. Clinical effects of NTCP-inhibitor myrcludex B. J. Viral Hepat. 28, 852–858. https://doi.org/10.1111/jvh.13490

ClusPro 2.0: protein-protein docking [WWW Document], n.d. URL https://cluspro.org/login.php (accessed 7.19.21).

Collins, D.S., Kourtis, L.C., Thyagarajapuram, N.R., Sirkar, R., Kapur, S., Harrison, M.W., Bryan, D.J., Jones, G.B., Wright, J.M., 2017. Optimizing the Bioavailability of Subcutaneously Administered Biotherapeutics Through Mechanochemical Drivers. Pharm. Res. 34, 2000–2011. https://doi.org/10.1007/s11095-017-2229-9

Coolen, A.-L., Lacroix, C., Mercier-Gouy, P., Delaune, E., Monge, C., Exposito, J.-Y., Verrier, B., 2019. Poly(lactic acid) nanoparticles and cell-penetrating peptide potentiate mRNA-based vaccine expression in dendritic cells triggering their activation. Biomaterials 195, 23–37. https://doi.org/10.1016/j.biomaterials.2018.12.019

Dalzon, B., Lebas, C., Jimenez, G., Gutjahr, A., Terrat, C., Exposito, J.-Y., Verrier, B., Lethias, C., 2016. Poly(Lactic Acid) Nanoparticles Targeting α5β1 Integrin as Vaccine Delivery Vehicle, a Prospective Study. PloS One 11, e0167663. https://doi.org/10.1371/journal.pone.0167663

De Silva, N.S., Klein, U., 2015. Dynamics of B cells in germinal centres. Nat. Rev. Immunol. 15, 137–148. https://doi.org/10.1038/nri3804

DeFranco, A.L., Rookhuizen, D.C., Hou, B., 2012. Contribution of TLR signaling to germinal center antibody responses. Immunol. Rev. 247, 64–72. https://doi.org/10.1111/j.1600-065X.2012.01115.x

Dembek, C., Protzer, U., Roggendorf, M., 2018. Overcoming immune tolerance in chronic hepatitis B by therapeutic vaccination. Curr. Opin. Virol. 30, 58–67. https://doi.org/10.1016/j.coviro.2018.04.003

Desmares, M., Delphin, M., Chardès, B., Pons, C., Riedinger, J., Michelet, M., Rivoire, M., Verrier, B., Salvetti, A., Lucifora, J., Durantel, D., 2022. Insights on the antiviral mechanisms of action of the TLR1/2 agonist Pam3CSK4 in hepatitis B virus (HBV)-infected hepatocytes. Antiviral Res. 206, 105386. https://doi.org/10.1016/j.antiviral.2022.105386

Dolgin, E., 2022. Closing in on a cure for hepatitis B. Nature 603, S46–S48. https://doi.org/10.1038/d41586-022-00812-1

Dou, Y., Jansen, D.T.S.L., van den Bosch, A., de Man, R.A., van Montfoort, N., Araman, C., van Kasteren, S.I., Zom, G.G., Krebber, W.-J., Melief, C.J.M., Woltman, A.M., Buschow, S.I., 2020. Design of TLR2-ligand-synthetic long peptide conjugates for therapeutic vaccination of chronic HBV patients. Antiviral Res. 178, 104746. https://doi.org/10.1016/j.antiviral.2020.104746

Du, G., Qin, M., Sun, X., 2022. Recent progress in application of nanovaccines for enhancing mucosal immune responses. Acta Pharm. Sin. B. https://doi.org/10.1016/j.apsb.2022.08.010

Durantel, D., Zoulim, F., 2016. New antiviral targets for innovative treatment concepts for hepatitis B virus and hepatitis delta virus. J. Hepatol., Molecular Biology of Hepatitis B Virus 64, S117–S131. https://doi.org/10.1016/j.jhep.2016.02.016

Fanning, G.C., Zoulim, F., Hou, J., Bertoletti, A., 2019. Therapeutic strategies for hepatitis B virus infection: towards a cure. Nat. Rev. Drug Discov. 18, 827–844. https://doi.org/10.1038/s41573-019-0037-0

Fries, C.N., Curvino, E.J., Chen, J.-L., Permar, S.R., Fouda, G.G., Collier, J.H., 2020. Advances in nanomaterial vaccine strategies to address infectious diseases impacting global health. Nat. Nanotechnol. https://doi.org/10.1038/s41565-020-0739-9

Glebe, D., Urban, S., Knoop, E.V., Cag, N., Krass, P., Grün, S., Bulavaite, A., Sasnauskas, K., Gerlich, W.H., 2005. Mapping of the hepatitis B virus attachment site by use of infection-inhibiting preS1 lipopeptides and tupaia hepatocytes. Gastroenterology 129, 234–245. https://doi.org/10.1053/j.gastro.2005.03.090

Graber-Stiehl, I., 2018. The silent epidemic killing more people than HIV, malaria or TB. Nature 564, 24–26. https://doi.org/10.1038/d41586-018-07592-7

Gripon, P., Rumin, S., Urban, S., Le Seyec, J., Glaise, D., Cannie, I., Guyomard, C., Lucas, J., Trepo, C., Guguen-Guillouzo, C., 2002. Infection of a human hepatoma cell line by hepatitis B virus. Proc. Natl. Acad. Sci. U. S. A. 99, 15655–15660. https://doi.org/10.1073/pnas.232137699

Gutjahr, A., Phelip, C., Coolen, A.-L., Monge, C., Boisgard, A.-S., Paul, S., Verrier, B., 2016. Biodegradable Polymeric Nanoparticles-Based Vaccine Adjuvants for Lymph Nodes Targeting. Vaccines 4. https://doi.org/10.3390/vaccines4040034

Harris, J.R., Markl, J., 1999. Keyhole limpet hemocyanin (KLH): a biomedical review. Micron 30, 597–623. https://doi.org/10.1016/S0968-4328(99)00036-0

Havenar-Daughton, C., Carnathan, D.G., Boopathy, A.V., Upadhyay, A.A., Murrell, B., Reiss, S.M., Enemuo, C.A., Gebru, E.H., Choe, Y., Dhadvai, P., Viviano, F., Kaushik, K., Bhiman, J.N., Briney, B., Burton, D.R., Bosinger, S.E., Schief, W.R., Irvine, D.J., Silvestri, G., Crotty, S., 2019. Rapid Germinal Center and Antibody Responses in Non-human Primates after a Single Nanoparticle Vaccine Immunization 35.

Havenar-Daughton, C., Lindqvist, M., Heit, A., Wu, J.E., Reiss, S.M., Kendric, K., Bélanger, S., Kasturi, S.P., Landais, E., Akondy, R.S., McGuire, H.M., Bothwell, M., Vagefi, P.A., Scully, E., Tomaras, G.D., Davis, M.M., Poignard, P., Ahmed, R., Walker, B.D., Pulendran, B., McElrath, M.J., Kaufmann, D.E., Crotty, S., 2016. CXCL13 is a plasma biomarker of germinal center activity. Proc. Natl. Acad. Sci. U. S. A. 113, 2702–2707. https://doi.org/10.1073/pnas.1520112113

Heise, N., De Silva, N.S., Silva, K., Carette, A., Simonetti, G., Pasparakis, M., Klein, U., 2014. Germinal center B cell maintenance and differentiation are controlled by distinct NF-κB

transcription factor subunits. J. Exp. Med. 211, 2103–2118. https://doi.org/10.1084/jem.20132613
Hennessy, E.J., Parker, A.E., O'Neill, L.A.J., 2010. Targeting Toll-like receptors: emerging therapeutics? Nat. Rev. Drug Discov. 9, 293–307. https://doi.org/10.1038/nrd3203
I-TASSER server for protein structure and function prediction [WWW Document], n.d. URL https://zhanglab.ccmb.med.umich.edu/I-TASSER/ (accessed 12.6.19).
Kardani, K., Bolhassani, A., Shahbazi, S., 2016. Prime-boost vaccine strategy against viral infections: Mechanisms and benefits. Vaccine 34, 413–423. https://doi.org/10.1016/j.vaccine.2015.11.062
Kasturi, S.P., Skountzou, I., Albrecht, R.A., Koutsonanos, D., Hua, T., Nakaya, H.I., Ravindran, R., Stewart, S., Alam, M., Kwissa, M., Villinger, F., Murthy, N., Steel, J., Jacob, J., Hogan, R.J., García-Sastre, A., Compans, R., Pulendran, B., 2011. Programming the magnitude and persistence of antibody responses with innate immunity. Nature 470, 543–547. https://doi.org/10.1038/nature09737
Kazanietz, M.G., Durando, M., Cooke, M., 2019. CXCL13 and Its Receptor CXCR5 in Cancer: Inflammation, Immune Response, and Beyond. Front. Endocrinol. 10. https://doi.org/10.3389/fendo.2019.00471
Kelly, H.G., Kent, S.J., Wheatley, A.K., 2019. Immunological basis for enhanced immunity of nanoparticle vaccines. Expert Rev. Vaccines 18, 269–280. https://doi.org/10.1080/14760584.2019.1578216
Kosinska, A.D., Bauer, T., Protzer, U., 2017. Therapeutic vaccination for chronic hepatitis B. Curr. Opin. Virol., Viral pathogenesis • Preventive and therapeutic vaccines 23, 75–81. https://doi.org/10.1016/j.coviro.2017.03.011
Lamalle-Bernard, D., Munier, S., Compagnon, C., Charles, M.-H., Kalyanaraman, V.S., Delair, T., Verrier, B., Ataman-Onal, Y., 2006. Coadsorption of HIV-1 p24 and gp120 proteins to surfactant-free anionic PLA nanoparticles preserves antigenicity and immunogenicity. J. Control. Release Off. J. Control. Release Soc. 115, 57–67. https://doi.org/10.1016/j.jconrel.2006.07.006
Lamrayah, M., Charriaud, F., Hu, S., Megy, S., Terreux, R., Verrier, B., 2019. Molecular modelling of TLR agonist Pam3CSK4 entrapment in PLA nanoparticles as a tool to explain loading efficiency and functionality. Int. J. Pharm. 568, 118569. https://doi.org/10.1016/j.ijpharm.2019.118569
Lamrayah, M., Phelip, C., Coiffier, C., Lacroix, C., Willemin, T., Trimaille, T., Verrier, B., 2022. A Polylactide-Based Micellar Adjuvant Improves the Intensity and Quality of Immune Response. Pharmaceutics 14, 107. https://doi.org/10.3390/pharmaceutics14010107
Lang, J., Neumann-Haefelin, C., Thimme, R., 2019. Immunological cure of HBV infection. Hepatol. Int. 13, 113–124. https://doi.org/10.1007/s12072-018-9912-8
Lavelle, E.C., Ward, R.W., 2022. Mucosal vaccines — fortifying the frontiers. Nat. Rev. Immunol. 22, 236–250. https://doi.org/10.1038/s41577-021-00583-2
Lee, G.-H., Lim, S.-G., 2021. CpG-Adjuvanted Hepatitis B Vaccine (HEPLISAV-B®) Update. Expert Rev. Vaccines 20, 487–495. https://doi.org/10.1080/14760584.2021.1908133
Lee, S.-H., Park, S.-R., 2018. Toll-like Receptor 1/2 Agonist Pam3CSK4 Suppresses Lipopolysaccharide-driven IgG1 Production while Enhancing IgG2a Production by B Cells. Immune Netw. 18. https://doi.org/10.4110/in.2018.18.e10
Li, J., Bao, M., Ge, J., Ren, S., Zhou, T., Qi, F., Pu, X., Dou, J., 2017. Research progress of therapeutic vaccines for treating chronic hepatitis B. Hum. Vaccines Immunother. 13, 986–997. https://doi.org/10.1080/21645515.2016.1276125
Lu, S., 2009. Heterologous prime-boost vaccination. Curr. Opin. Immunol. 21, 346–351. https://doi.org/10.1016/j.coi.2009.05.016
Lucifora, J., Bonnin, M., Aillot, L., Fusil, F., Maadadi, S., Dimier, L., Michelet, M., Floriot, O., Ollivier, A., Rivoire, M., Ait-Goughoulte, M., Daffis, S., Fletcher, S.P., Salvetti, A., Cosset, F.-L., Zoulim, F., Durantel, D., 2018. Direct antiviral properties of TLR ligands against HBV replication in immune-competent hepatocytes. Sci. Rep. 8, 5390. https://doi.org/10.1038/s41598-018-23525-w
Marion, M.-J., Hantz, O., Durantel, D., 2010. The HepaRG Cell Line: Biological Properties and Relevance as a Tool for Cell Biology, Drug Metabolism, and Virology Studies, in: Maurel, P. (Ed.), Hepatocytes: Methods and Protocols, Methods in Molecular Biology. Humana Press, Totowa, NJ, pp. 261–272. https://doi.org/10.1007/978-1-60761-688-7_13

Megy, S., Aguero, S., Da Costa, D., Lamrayah, M., Berthet, M., Primard, C., Verrier, B., Terreux, R., 2020. Molecular Dynamics Studies of Poly(Lactic Acid) Nanoparticles and Their Interactions with Vitamin E and TLR Agonists Pam1CSK4 and Pam3CSK4. Nanomaterials 10, 2209. https://doi.org/10.3390/nano10112209
Meier, A., Mehrle, S., Weiss, T.S., Mier, W., Urban, S., 2013. Myristoylated PreS1-domain of the hepatitis B virus L-protein mediates specific binding to differentiated hepatocytes. Hepatol. Baltim. Md 58, 31–42. https://doi.org/10.1002/hep.26181
Meng, Z., Chen, Y., Lu, M., 2019. Advances in Targeting the Innate and Adaptive Immune Systems to Cure Chronic Hepatitis B Virus Infection. Front. Immunol. 10, 3127. https://doi.org/10.3389/fimmu.2019.03127
Mitchell, M.J., Billingsley, M.M., Haley, R.M., Wechsler, M.E., Peppas, N.A., Langer, R., 2020. Engineering precision nanoparticles for drug delivery. Nat. Rev. Drug Discov. 1–24. https://doi.org/10.1038/s41573-020-0090-8
Monrad, J.T., Sandbrink, J.B., Cherian, N.G., 2021. Promoting versatile vaccine development for emerging pandemics. Npj Vaccines 6, 1–7. https://doi.org/10.1038/s41541-021-00290-y
Ni, Y., Lempp, F.A., Mehrle, S., Nkongolo, S., Kaufman, C., Fälth, M., Stindt, J., Königer, C., Nassal, M., Kubitz, R., Sültmann, H., Urban, S., 2014. Hepatitis B and D viruses exploit sodium taurocholate co-transporting polypeptide for species-specific entry into hepatocytes. Gastroenterology 146, 1070–1083. https://doi.org/10.1053/j.gastro.2013.12.024
Park, H., Bradley, P., Greisen, P., Liu, Y., Mulligan, V.K., Kim, D.E., Baker, D., DiMaio, F., 2016. Simultaneous Optimization of Biomolecular Energy Functions on Features from Small Molecules and Macromolecules. J. Chem. Theory Comput. 12, 6201–6212. https://doi.org/10.1021/acs.jctc.6b00819
Pavot, V., Climent, N., Rochereau, N., Garcia, F., Genin, C., Tiraby, G., Vernejoul, F., Perouzel, E., Lioux, T., Verrier, B., Paul, S., 2016. Directing vaccine immune responses to mucosa by nanosized particulate carriers encapsulating NOD ligands. Biomaterials 75, 327–339. https://doi.org/10.1016/j.biomaterials.2015.10.034
Pavot, V., Rochereau, N., Primard, C., Genin, C., Perouzel, E., Lioux, T., Paul, S., Verrier, B., 2013. Encapsulation of Nod1 and Nod2 receptor ligands into poly(lactic acid) nanoparticles potentiates their immune properties. J. Control. Release Off. J. Control. Release Soc. 167, 60–67. https://doi.org/10.1016/j.jconrel.2013.01.015
Pedersen, G.K., Wørzner, K., Andersen, P., Christensen, D., 2020. Vaccine Adjuvants Differentially Affect Kinetics of Antibody and Germinal Center Responses. Front. Immunol. 11. https://doi.org/10.3389/fimmu.2020.579761
Peplow, M., 2021. Nanotechnology offers alternative ways to fight COVID-19 pandemic with antivirals. Nat. Biotechnol. 39, 1172–1174. https://doi.org/10.1038/s41587-021-01085-1
Peres, C., Matos, A.I., Conniot, J., Sainz, V., Zupančič, E., Silva, J.M., Graça, L., Sá Gaspar, R., Préat, V., Florindo, H.F., 2017. Poly(lactic acid)-based particulate systems are promising tools for immune modulation. Acta Biomater. 48, 41–57. https://doi.org/10.1016/j.actbio.2016.11.012
Polaris Observatory Collaborators, 2018. Global prevalence, treatment, and prevention of hepatitis B virus infection in 2016: a modelling study. Lancet Gastroenterol. Hepatol. 3, 383–403. https://doi.org/10.1016/S2468-1253(18)30056-6
Pulendran, B., 2009. Learning immunology from the yellow fever vaccine: innate immunity to systems vaccinology. Nat. Rev. Immunol. 9, 741–747. https://doi.org/10.1038/nri2629
Pulendran, B., Ahmed, R., 2011. Immunological mechanisms of vaccination. Nat. Immunol. 12, 509–517. https://doi.org/10.1038/ni.2039
Pulendran, B., S. Arunachalam, P., O'Hagan, D.T., 2021. Emerging concepts in the science of vaccine adjuvants. Nat. Rev. Drug Discov. 1–22. https://doi.org/10.1038/s41573-021-00163-y
Qiao, D., Chen, Y., Liu, L., 2021. Engineered therapeutic nanovaccine against chronic hepatitis B virus infection. Biomaterials 269, 120674. https://doi.org/10.1016/j.biomaterials.2021.120674
Qin, Y., Liao, P., 2018. Hepatitis B virus vaccine breakthrough infection: surveillance of S gene mutants of HBV. Acta Virol. 62, 115–121. https://doi.org/10.4149/av_2018_210
Rammensee, H.-G., Wiesmüller, K.-H., Chandran, P.A., Zelba, H., Rusch, E., Gouttefangeas, C., Kowalewski, D.J., Di Marco, M., Haen, S.P., Walz, J.S., Gloria, Y.C., Bödder, J., Schertel, J.-M., Tunger, A., Müller, L., Kießler, M., Wehner, R., Schmitz, M., Jakobi, M.,

Schneiderhan-Marra, N., Klein, R., Laske, K., Artzner, K., Backert, L., Schuster, H., Schwenck, J., Weber, A.N.R., Pichler, B.J., Kneilling, M., la Fougère, C., Forchhammer, S., Metzler, G., Bauer, J., Weide, B., Schippert, W., Stevanović, S., Löffler, M.W., 2019. A new synthetic toll-like receptor 1/2 ligand is an efficient adjuvant for peptide vaccination in a human volunteer. J. Immunother. Cancer 7, 307. https://doi.org/10.1186/s40425-019-0796-5

Rességuier, J., Delaune, E., Coolen, A.-L., Levraud, J.-P., Boudinot, P., Le Guellec, D., Verrier, B., 2017. Specific and Efficient Uptake of Surfactant-Free Poly(Lactic Acid) Nanovaccine Vehicles by Mucosal Dendritic Cells in Adult Zebrafish after Bath Immersion. Front. Immunol. 8, 190. https://doi.org/10.3389/fimmu.2017.00190

Saco, T.V., Strauss, A.T., Ledford, D.K., 2018. Hepatitis B vaccine nonresponders: Possible mechanisms and solutions. Ann. Allergy Asthma Immunol. Off. Publ. Am. Coll. Allergy Asthma Immunol. 121, 320–327. https://doi.org/10.1016/j.anai.2018.03.017

Schudel, A., Francis, D.M., Thomas, S.N., 2019. Material design for lymph node drug delivery. Nat. Rev. Mater. 4, 415–428. https://doi.org/10.1038/s41578-019-0110-7

Singh, A., 2021. Eliciting B cell immunity against infectious diseases using nanovaccines. Nat. Nanotechnol. 16, 9.

Singh, M., Chakrapani, A., O'Hagan, D., 2007. Nanoparticles and microparticles as vaccine-delivery systems. Expert Rev. Vaccines 6, 797–808. https://doi.org/10.1586/14760584.6.5.797

Swaminathan, A., Lucas, R.M., Dear, K., McMichael, A.J., 2014. Keyhole limpet haemocyanin - a model antigen for human immunotoxicological studies. Br. J. Clin. Pharmacol. 78, 1135–1142. https://doi.org/10.1111/bcp.12422

Urban, S., Bartenschlager, R., Kubitz, R., Zoulim, F., 2014. Strategies to inhibit entry of HBV and HDV into hepatocytes. Gastroenterology 147, 48–64. https://doi.org/10.1053/j.gastro.2014.04.030

van Zundert, G.C.P., Rodrigues, J.P.G.L.M., Trellet, M., Schmitz, C., Kastritis, P.L., Karaca, E., Melquiond, A.S.J., van Dijk, M., de Vries, S.J., Bonvin, A.M.J.J., 2016. The HADDOCK2.2 Web Server: User-Friendly Integrative Modeling of Biomolecular Complexes. J. Mol. Biol. 428, 720–725. https://doi.org/10.1016/j.jmb.2015.09.014

Varkhede, N., Bommana, R., Schöneich, C., Forrest, M.L., 2020. Proteolysis and Oxidation of Therapeutic Proteins After Intradermal or Subcutaneous Administration. J. Pharm. Sci. 109, 191–205. https://doi.org/10.1016/j.xphs.2019.08.005

Victora, G.D., Nussenzweig, M.C., 2012. Germinal Centers. Annu. Rev. Immunol. 30, 429–457. https://doi.org/10.1146/annurev-immunol-020711-075032

Wang, W., Zhou, X., Bian, Y., Wang, S., Chai, Q., Guo, Z., Wang, Z., Zhu, P., Peng, H., Yan, X., Li, W., Fu, Y.-X., Zhu, M., 2020. Dual-targeting nanoparticle vaccine elicits a therapeutic antibody response against chronic hepatitis B. Nat. Nanotechnol. 15, 406–416. https://doi.org/10.1038/s41565-020-0648-y

Yan, H., Zhong, G., Xu, G., He, W., Jing, Z., Gao, Z., Huang, Y., Qi, Y., Peng, B., Wang, H., Fu, L., Song, M., Chen, P., Gao, W., Ren, B., Sun, Y., Cai, T., Feng, X., Sui, J., Li, W., 2012. Sodium taurocholate cotransporting polypeptide is a functional receptor for human hepatitis B and D virus. eLife 1, e00049. https://doi.org/10.7554/eLife.00049

Yato, K., Onodera, T., Matsuda, M., Moriyama, S., Fujimoto, A., Watashi, K., Aizaki, H., Tanaka, T., Moriishi, K., Nishitsuji, H., Shimotohno, K., Tamura, K., Takahashi, Y., Wakita, T., Muramatsu, M., Kato, T., Suzuki, R., 2020. Identification of Two Critical Neutralizing Epitopes in the Receptor Binding Domain of Hepatitis B Virus preS1. J. Virol. https://doi.org/10.1128/JVI.01680-20

Ye, X., Zhou, M., He, Y., Wan, Y., Bai, W., Tao, S., Ren, Y., Zhang, X., Xu, J., Liu, J., Zhang, J., Hu, K., Xie, Y., 2016. Efficient Inhibition of Hepatitis B Virus Infection by a preS1-binding Peptide. Sci. Rep. 6, 29391. https://doi.org/10.1038/srep29391

Zhu, D.D., Zhang, X.P., Yu, H.L., Liu, R.X., Shen, C.B., Zhang, W.F., Cui, Y., Guo, X.D., 2019. Kinetic stability studies of HBV vaccine in a microneedle patch. Int. J. Pharm. 567, 118489. https://doi.org/10.1016/j.ijpharm.2019.118489